sustainability

Article

Low Nickel, Ceria Zirconia-Based Micro-Tubular Solid Oxide Fuel Cell: A Study of Composition and Oxidation Using Hydrogen and Methane Fuel

Hazrul Adzfar Shabri [1], Siti Norlaila Faeizah Mohd Rudin [2], Shahirah Deraman [1], Mazlinda Ab Rahman [1], Mohd Hafiz Dzarfan Othman [3,*], Siti Munira Jamil [4], Tonni Agustiono Kurniawan [5], Tao Li [6], Suriani Abu Bakar [7], Nafisah Osman [8], Juhana Jaafar [3], Mukhlis A Rahman [3] and Ahmad Fauzi Ismail [3]

[1] Advanced Membrane Technology Research Centre (AMTEC), Universiti Teknologi Malaysia, Skudai 81310, Malaysia; hazrul.adzfar@graduate.utm.my (H.A.S.); shahirahderaman23@gmail.com (S.D.); mazlindaabrahman@gmail.com (M.A.R.)
[2] Process System Engineering Center (PROSPECT), Universiti Teknologi Malaysia, Skudai 81310, Malaysia; snfaeizah2@graduate.utm.my
[3] Department of Energy Engineering, School of Chemical and Energy Engineering (FCEE), Universiti Teknologi Malaysia, Skudai 81310, Malaysia; juhana@petroleum.utm.my (J.J.); mukhlis@petroleum.utm.my (M.A.R.); afauzi@utm.my (A.F.I.)
[4] School of Professional and Continuing Education (SPACE), Universiti Teknologi Malaysia, Skudai 81310, Malaysia; sitimunira@utmspace.edu.my
[5] Key Laboratory of the Coastal and Wetland Ecosystems (Xiamen University), Ministry of Education, College of Environment and Ecology, Xiamen University, Xiamen 361102, China; tonni@xmu.edu.cn
[6] School of Energy & Environment, Southeast University, Nanjing 210096, China; 101012902@seu.edu.cn
[7] Nanotechnology Research Centre, Faculty of Science and Mathematics, Universiti Pendidikan Sultan Idris, Tanjung Malim 35900, Malaysia; suriani@fsmt.upsi.edu.my
[8] Fakulti Sains Gunaan, Universiti Teknologi MARA Cawangan Perlis, Kampus Arau, Arau 02600, Malaysia; fisha@perlis.uitm.edu.my
* Correspondence: hafiz@petroleum.utm.my

Citation: Shabri, H.A.; Rudin, S.N.F.M.; Deraman, S.; Rahman, M.A.; Othman, M.H.D.; Jamil, S.M.; Kurniawan, T.A.; Li, T.; Bakar, S.A.; Osman, N.; et al. Low Nickel, Ceria Zirconia-Based Micro-Tubular Solid Oxide Fuel Cell: A Study of Composition and Oxidation Using Hydrogen and Methane Fuel. *Sustainability* **2021**, *13*, 13789. https://doi.org/10.3390/su132413789

Academic Editor: Thanikanti Sudhakar Babu

Received: 14 November 2021
Accepted: 11 December 2021
Published: 14 December 2021

Abstract: The study examines the effect of using low nickel (Ni) with high ceria (CeO_2) anode content towards the oxidation of H_2 and CH_4 fuel by evaluating the activation energy of the ohmic process and charge transfer process. Using a micro-tubular solid oxide fuel cell (MT-SOFC), the anodes are made up of 50% YSZ with varying NiO:CeO_2 percentages from 0% NiO, 50% CeO_2 to 50% NiO, 0% CeO_2. The performance is measured based on maximum power density (MPD), electrochemical impedance spectroscopy (EIS) and activation energy, E_a of the ohmic (Rohm) and charge transfer (R_{ct}) processes. We found that by lowering the Ni content to lower than 50% NiO, anode conductivity will drop by 7-fold. An anode containing 37.5% NiO, 12.5% CeO_2 yield MPD of 41.1 and 2.9 mW cm^{-2} when tested on H_2 and CH_4 fuels thus have the lowest Ni content without an abrupt negative effect on the MPD and EIS. The significant effect of conductivity drops on MPD and EIS are observed to occur at 25% NiO, 25% CeO_2 and lower NiO content. However, anode content of 25% NiO, 25% CeO_2 has the lowest E_a for R_{ct} (29.74 kJ mol^{-1}) for operation in CH_4, making it the best anode composition to oxidize CH_4. As a conclusion, an anode containing 25% NiO:25% CeO_2:50% YSZ and 37.5% NiO:12.5% CeO_2:50% YSZ shows promising results in becoming the low Ni anode for coking-tolerant SOFC.

Keywords: microtubular solid oxide fuel cell; ceria; methane; nickel; coking resistant; YSZ

1. Introduction

The emission of greenhouse gases, mainly carbon dioxide, from fossil fuel burning has led to climate changes where the global average temperature has been rising by 0.08 °C per decade since 1880 [1]. This emission is mainly attributed to electricity generation by coal burning, involving multiple steps of energy conversion. The stored chemical energy in fuel is changed to heat, then mechanical, and later, electrical energy, losing a small portion of energy due to inefficiency in the energy exchanging process in each step.

Hydrocarbon fuel is being actively researched as a fuel for solid oxide fuel cells (SOFCs) due to the high operating temperature of SOFC that sits well in the hydrocarbon reforming region. Producing electricity by means of a fuel cell involves only one step, potentially limiting energy losses due to inefficiency in multiple steps. The well-known challenge associated with nickel-cermet anodes with hydrocarbon fuel is the coking of the anode or carbon deposition on the surface of the anode [2]. The problem existed due to Ni's tendency of nucleating carbon growth, which also explains its function as one of the dehydrogenation catalysts in other processes [3].

Coking eventually blocks the anode for further contact and reaction with reactant gas fuels, thus reducing the performance over time. Subsequently, ceria or CeO_2 is actively researched as a possible carbon oxidation catalyst to mitigate this issue. The catalytic properties of CeO_2 are well-known as it is used as a catalyst in a catalytic converter to oxidize unburned hydrocarbon in vehicles' emissions [4]. The recently landed Mars Perseverance Rover on Mars even carried an onboard solid oxide electrolyzer cell (SOEC) with an electrode made up of Ni–YSZ and Ni–CeO_2 to produce O_2 from CO_2 [5].

CeO_2 used in an SOFC study can be in the form of pure or doped CeO_2, such as gadolinium doped ceria (GDC) and samarium doped ceria (SDC). Use of doped CeO_2 is more favorable due to higher oxide ion conductivity compared to pure ceria, which also made them a common electrolyte material as well. Studies using a doped GDC electrolyte have shown a maximum power density (MPD) of 0.67 to 1.7 W cm^{-2} on H_2 fuel and 0.13 to 1.4 W cm^{-2} on CH_4 [6–8].

On the other hand, the usage of ceria is still favorable compared to doped ceria due to its lower cost. Additionally, SOFC based on doped ceria as an electrolyte (termed as intermediate temperature-SOFC due to lower operating temperature) suffers current leakage due to the tendency of Ce(IV) to be reduced to Ce(III) in highly reducing environments. This unwanted reduction occurs during anode reduction processes or prolonged operation, which creates n-type conductivity in the electrolyte, lowering performances [9]. Furthermore, doped ceria such as samarium doped ceria (SDC) used as electrolyte material was shown to exhibit different catalytic properties compared to ceria deposited as an anode [10].

Currently, most methods employed in creating a ceria-loaded Ni–YSZ anode of a micro-tubular solid oxide fuel cell (MT-SOFC) involve infusing soluble cerium salt such as cerium nitrate followed by calcination and oxidation to turn the cerium to cerium oxide [11,12]. This method managed to produce an MPD of 0.283 to 0.55 Wcm^{-2} on H_2 fuel and 0.16 to 0.241 Wcm^{-2} on CH_4 at 900 °C, respectively [11,12]. Whilst this method was shown to be successful in creating a low-ceria-content Ni–YSZ anode, higher ceria content in a Ni–YSZ anode is harder to be fabricated due to the increasing number of deposition cycles. Furthermore, the oxidation of the soluble cerium metal to form CeO_2 sometimes also produces other forms of cerium oxides, mainly Ce_2O_3. Furthermore, to our knowledge, there is no study that employs the direct use of CeO_2 into an anode of MT-SOFC. Thus, in this paper, we explored another potential of a high-CeO_2-content Ni–YSZ anode of MT-SOFC in order to create a coking-tolerant SOFC anode. In this method, CeO_2 was directly added during single-step fabrication of an anode/electrolyte dual-layer hollow fiber in order to avoid the two-step process, i.e., repetitive deposition process and sintering.

Micro-tubular solid oxide fuel cell (MT-SOFC) is gaining attention as one of the candidates to commercialize SOFC as opposed to traditional planar SOFC [13]. In MT-SOFC, the tubular form consisting of an anode, electrolyte and cathode was fabricated in less time with lower costs than the planar SOFC and had a micron-size lumen and thinner anode, thus having higher performance compared to planar SOFC. MT-SOFC may be fabricated using a phase inversion process, followed by calcination and sintering at high temperatures. One, two or even three layers can even be fabricated together, creating a single-layer, dual-layer [14] or triple-layer (TL) hollow fiber (HF) [15]. For example, the anode and electrolyte layer can be fabricated together in dual-layer hollow fiber (DL-HF) and complete cells of anode, electrolyte and cathode can be fabricated as a triple-layer hollow fiber (TL-HF).

In anodes, the charge transfer process involves a reaction between oxide ion and fuel that leads to oxidation of the fuel and release of electrons, which generates electricity. The study of the charge transfer process is important since the process depends greatly on the catalytic properties of the anode material [10]. Similar to every other chemical process, reactions between fuel and oxide ions on the anode surface require the reactant to overcome an energy barrier, termed activation energy or E_a. Lower E_a will result in more reactants having minimum energy requirements and hence more reactions occurring, thus increasing the current density of the fuel cell. Investigating the E_a value of the charge transfer process can be achieved via an Arrhenius plot of the R_{ct} value at different operating temperatures.

The objective of this study is to investigate the effect of CeO_2 and Ni content in the anode of MT-SOFC on that of the oxidation of H_2 and CH_4 fuel by using evaluation of the activation energy of the ohmic process and charge transfer process. Unlike other studies, CeO_2 was fabricated together with the NiO–YSZ anode to produce the Ni–CeO_2–YSZ anode with a YSZ electrolyte. The two layers were fabricated together in the form of dual-layer hollow fiber using a co-extrusion-based phase inversion process. The MT-SOFC uses pure YSZ electrolytes, and the anode is composed of 50% YSZ, with the remaining 50% made up of mixtures of Ni and CeO_2. The Ni and CeO_2 content were varied to investigate the effect of the Ni and CeO_2 content on the physical structure such as morphology, gas permeability and mechanical strength. The effect was also investigated in terms of anode conductivity, power density and impedance spectroscopy in H_2 and CH_4 fuel at varying temperatures. Finally, analysis of activation energy, E_a, by means of an Arrhenius plot was performed on the ohmic resistance, R_{ohm}, and charge transfer resistance, R_{ct}, from the EIS of the SOFC obtained at temperatures from 700 to 900 °C on H_2 and CH_4 fuel. This is to examine the effect of temperature on the ohmic and charge transfer process of the varying Ni and CeO_2 content. The produced MT-SOFC was expected to increase the performance of MT-SOFC on operating with CH_4 fuel while using a low content of Ni. This work will enable MT-SOFC to operate stably using methane fuel, which can later be extended to hydrocarbon-based renewable fuel such as biogas as well.

2. Methodology

2.1. Materials

Commercially available 8% molar yttria-stabilized zirconia (YSZ) with a size of 0.35–0.45 µm and surface area 9 $m^2\ g^{-1}$, nickel oxide (NiO) with a size of 0.5–1.5 µm and surface area 5 $m^2\ g^{-1}$, and lanthanum strontium manganite, $(La_{0.80}Sr_{0.20})_{0.95}MnO_{3-\delta}$ (LSM) with a surface area 10.9 $m^2\ g^{-1}$ were obtained from NexTech Material Ltd. (Columbus, OH, USA). Cerium (IV) oxide (CeO_2) with size <5 µm was obtained from Sigma Aldrich. N-methyl-2-pyrrolidone (NMP) (Sigma Aldrich (M) Sdn. Bhd, Petaling Jaya, Malaysia) was used as the solvent while polyethyleneglycol 30-dipolyhydroxystearate (Arlacel P135) (Uniqema, Goole, UK) and polyethersulfone, (PES, Radel A-300) (Solvay, Shanghai, China) were used as the dispersant and polymer binder, respectively. Tap water was used as both internal and external coagulants.

2.2. Fabrication of DL-HF

The fabrication of anode/electrolyte DL-HF was performed as mentioned in [13,14]. Briefly, the suspension of the inner and outer layer of DL-HF was prepared separately. The outer layer made up the electrolyte layer entirely and consists of YSZ, while the inner layer formed the anode layer and was made up of mixtures of NiO, CeO_2 and YSZ as the ceramic component, as shown in Table 1. Five compositions of anodes were prepared with varying NiO and CeO_2 content, named Mat_A, Mat_B, Mat_C, Mat_D and Mat_E.

Table 1. Ceramic composition sample of anode (weight percentage).

Sample Name	NiO, %	CeO_2, %	YSZ, %
Mat_A	0	50	50
Mat_B	12.5	37.5	50
Mat_C	25	25	50
Mat_D	37.5	12.5	50
Mat_E	50	0	50

The electrolyte layer was made of 100YSZ as the ceramic component. The suspension was made up of 65% ceramic, 6.5% polyethylethersulfone (PESf) as polymer binder, 0.12% Arlacel P135 as surfactant and 28.38% N-Methyl-2-pyrrolidone (NMP) as solvent. The ceramic components were mixed with the solvent and dispersant in a planetary ball milling machine (Magna Value), then ball milled for 24 h, followed by the addition of polymer binder and further ball milled for 24 h. The suspensions were pumped through an orifice opening called spinneret, as shown in Figure A1 in Appendix A.

The flow rates used were 3, 10 and 10 mL min^{-1} each for the outer layer, inner layer and water acting as an internal coagulant into the water bath, which acts as external coagulant at an air gap of 10 cm. Phase inversion follows in which solvent/non-solvent exchange occurred, leaving a solidified polymer phase with ceramic powders. The produced material, called DL-HFs, was soaked in the water and air-dried for 24 h. Then, the produced DL-HF was calcined at 600 °C for 1 h (ramp up rate = 5 °C min^{-1}) followed by sintering at 1450 °C for 8 h (ramp up rate 10 °C min^{-1}, ramp down rate 5 °C min^{-1}) using a tube furnace (Magna Value). Both calcination and sintering were performed using air as the atmosphere. These ceramic DL-HFs produced were subjected to characterization analysis.

2.3. Characterization

Unreduced ceramic DL-HFs were scanned using SEM-EDX (Hitachi TM3030) to examine the morphology and the distribution of elements in the sample. The samples were carefully snapped in the middle and mounted onto a sample holder to examine the cross section view of the ceramic DL-HFs. Images and EDX elemental mapping were taken at a magnification of 60× for the overall cross section shape, 500× to examine the layering of the electrolyte and anode and 1500× at the anode to examine the microstructure. The samples were then crushed and tested with X-ray Diffraction (XRD) using Rigaku Smart Lab to examine the crystallinity structure of the Ni–CeO_2–YSZ material. Similarly, the structure of the reduced Mat_C DL-HF was scanned using XRD to examine the reducibility of Ni and the effect of reduction on the reducibility of CeO_2.

Gas permeation tests were performed on the unreduced and reduced anode layer as performed by [13,14]. To perform this, the sample was mounted on 3/8″ tube-thread male connectors, as shown in Figure A2 in Appendix A using epoxy resin. The sample was fitted to a permeation cell where the flow rate of N_2 gas flowing through the anode was measured using a bubble flow meter at varying inlet pressures.

Gas permeability was determined from Equation (1), where P is the value of gas permeability (mol m^{-2} s^{-1} Pa^{-1}). Q, D_i, D_o, L and P are each gas permeation rate (mol s^{-1}), inner diameter (m), outer diameter (m), length of hollow fiber (m) and pressure difference (P).

$$P = \frac{Q\ln(D_o/D_i)}{\pi L(D_o - D_i \Delta P)} \tag{1}$$

Mechanical strength of the ceramic DL-HF was measured via the Modulus of Rupture (MOR) method using mechanical testing equipment INSTRON 8032, as performed by [13,14]. This is to examine the effect of the sintering temperature and anode composition on the strength of the fiber. The sample was placed between two supports at a distance of

5 cm each, as shown in Figure A3 in Appendix A. The load was applied by the machine, and the bending strength was calculated using Equation (2) below.

$$B_F = \frac{8\ NLD_c}{\pi\left(D_o^4 - D_i^4\right)} \tag{2}$$

where N is the load value when the break occurs.

2.4. Conductivity Test

The electrical conductivity of the single-layer anode was measured using a 2-point direct-current (DC) technique using a potentiostat/galvanostat (Autolab PGSTAT 30, Eco-Chemie, The Netherlands). Potential between 0 and 1 V was applied across WE/S and RE/CE, and the resultant current was measured. The voltage–current plot was made, where the slope was taken as resistance, ρ_a. The conductivities were calculated according to Equation (3).

$$\sigma = \frac{L}{\rho_a\ A} \tag{3}$$

where σ = conductivities, S cm^{-1}, L = length of fiber, cm, ρ_a = resistance, A = area. $A = \pi\ (D_o{}^2 - D_i{}^2)/4$.

The plot of conductivities against percentage by volume, % volume Ni were plotted. The value of percentage by volume were obtained by dividing the mass with density for each component.

2.5. Performance Test

Finally, for the performance test, the ceramic DL-HF was coated with a cathode via a paint brush technique consisting of 3 layers where the first and second layers were 50% LSM and 50% YSZ, and the third layer was 100% LSM. The cathode material was prepared in suspension made of equal weight propylene glycol. The cell is sintered similarly as before but at 1250 °C sintering temperature.

To test for electrochemical performance, completed cells consisting of an anode, electrolyte and cathode were mounted onto the setup, as shown in Figure A4 in Appendix A. To perform this, silver wire was passed through the lumen or the anode side of the completed cells while another silver wire was wrapped around the cathode, as shown in Figure A4. The completed cells were mounted onto two alumina tubes at each end and sealed with a ceramic sealant (Aremco Ceramabond 552).

The anode collecting wire was connected to the WE/S electrode of PGSTAT as in the conductivity test, while the cathode collecting wire was connected to the RE/CE electrode. Fuel gas was passed through the lumen of the completed cells, while air was used as the oxidant on the cathode side. The cells were tested using H_2 and CH_4 gas at 10 mL min^{-1} at 700, 750, 800, 850 and 900 °C. At each fuel and temperature, maximum power density (MPD) was obtained by testing the cell for the current–voltage (I-V) curve. The completed cells were also tested for electrochemical impedance spectroscopy (EIS). From the EIS result, the ohmic resistance (R_{ohm}) was obtained by measuring the distance on the real axis from 0 to the left side of the first semicircle on the Nyquist plot, and the charge transfer resistance (R_{ct}) was measured as the diameter of the semicircle on the real axis. These values were subsequently plotted in the Arrhenius plot to investigate the activation energy (R_a) of the ohmic and charge transfer process.

3. Results and Discussion

3.1. Morphology and Properties

SEM imaging and EDX mapping of the cross section of the ceramic DL-HFs are shown in Figure 1. Based on Figure 1i,ii, the finger-like voids were present in all of the DL-HFs. The finger-like voids have been observed and reported in all of the studies, producing hollow fibers using a phase inversion/co-extrusion method and Ni-GDC and Ni–YSZ [8,15].

Finger-like formation occurs due to the phase inversion process between the water-soluble phase in the internal and external coagulant phase and the solvent-polymer phase in the suspension. The movement of the solvent NMP from suspension into the water caused the remaining ceramic polymer to solidify. The affinity of the NMP towards water and ceramic-polymer determines the structure of the solid ceramic-polymer formed. Since different ceramic components are known to have different affinities towards NMP, different ceramic materials will cause different formations, sometimes with undesirable effects. However, in this study, it was found that a finger-like formation with a sponge-like structure is well-formed in the NiO–CeO_2–YSZ anode and in the electrolyte. This geometry was formed since both the anode and electrolyte layers were in contact with water during the phase inversion process.

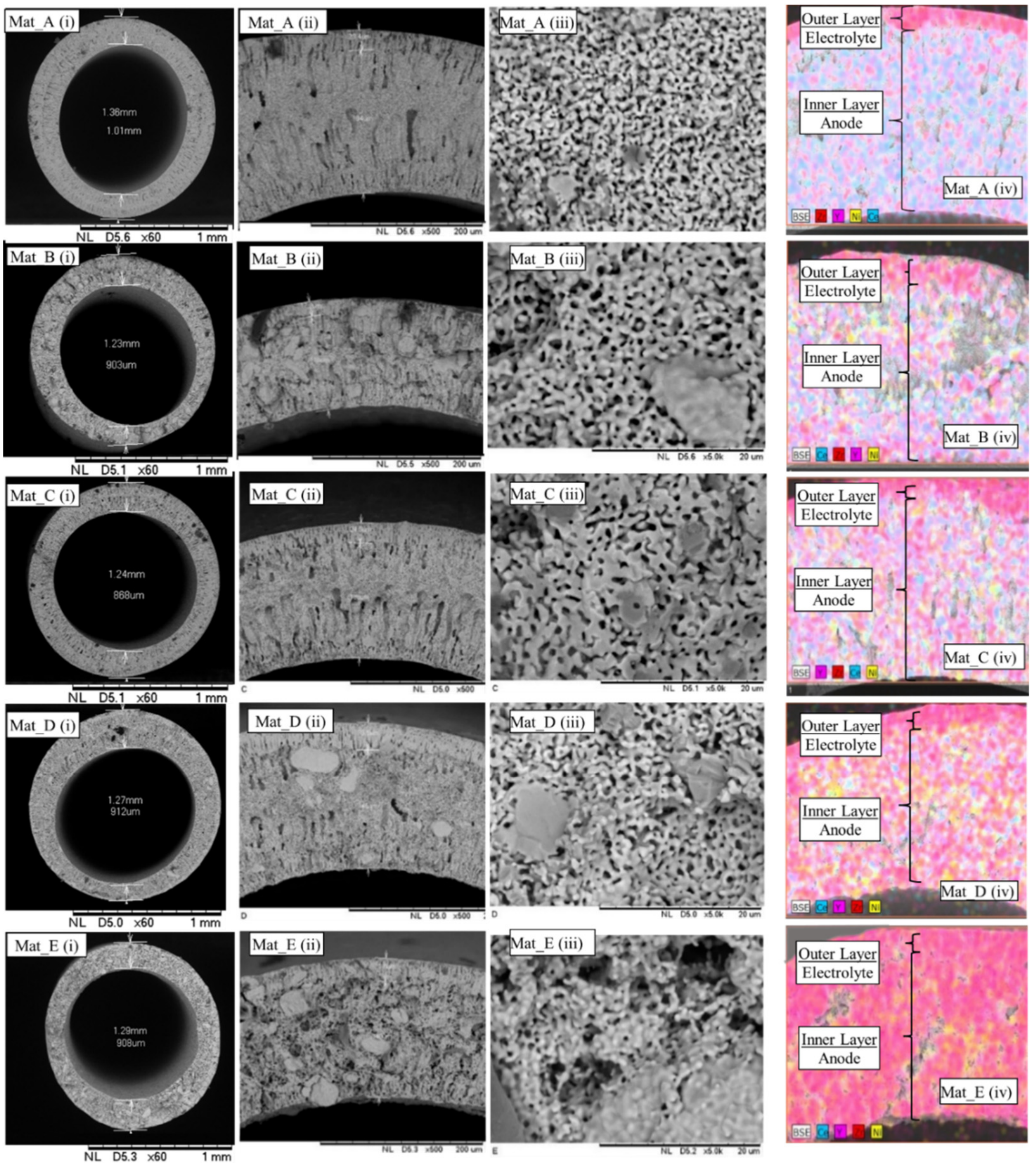

Figure 1. Ceramic DL-HF showing the external layer of the electrolyte and internal layer of the anode. Magnification is (**i**) 60×, (**ii**) 500× and (**iii**) 1500× at the inner layer anode, (**iv**) 60× with the EDX elemental mapping.

The finger-like formation created a large porose structure with a diameter of around 1 micrometer, while the sponge-like structure gave submicron porosity to the structure. Based on Figure 1i, the average DL-HF obtained have diameters ranging from 1.23 to

1.36 mm with lumen from 0.868 to 1.01 mm. The electrolyte thicknesses ranged from 23.4 to 27 µm, which was preferable since the reduced thickness ensures lower resistance towards the flow of oxygen ions [16].

High magnification images of 1500× were taken for all of the fibers, as shown in Figure 1iii, to examine the morphologies at the grain level. Large chunks of matter were found to present increasingly in size from Mat_A to Mat_E in the anode layer. EDX mapping, as shown in Figure 1iv, shows that the large chunks consist mainly of Y and Zr elements. Thus, it was found that the YSZ had sintered and agglomerated into larger chunks as the content of NiO increased (or CeO_2 decreased). Based on XRD results in the next section, YSZ was found to form a new phase with CeO_2 forming multiple ceria–zirconia phases. In low NiO content or high CeO_2 content, the YSZ formed a uniform ceria–zirconia structure without large chunks of YSZ. However, in high NiO content or low CeO_2 content, the YSZ agglomerated together to form a larger YSZ structure.

An X-ray diffraction study on unreduced Mat_A, Mat_B, Mat_C, Mat_D and Mat_E is shown in Figure 2a. Based on Figure 2a, in Mat_A (50% YSZ, 50% CeO_2 anode), the XRD result shows a major peak of YSZ and CeO_2, whilst the minor peaks of the phases of ceria–zirconia ($CeZrO_4$) are present as found using the database search. The major sharp peaks of YSZ were expected to come from the electrolyte and anode layers. Little of the CeO_2 content, however, was found to enter the lattice of the ZrO_2 in YSZ to create the ceria–zirconia compound. This event was observed when zirconia and ceria were present and sintered at high temperatures in another study [17]. In Mat_E, however, the NiO and YSZ mixture was not found to produce another phase, as shown in Figure 2a (50% YSZ, 50% NiO anode).

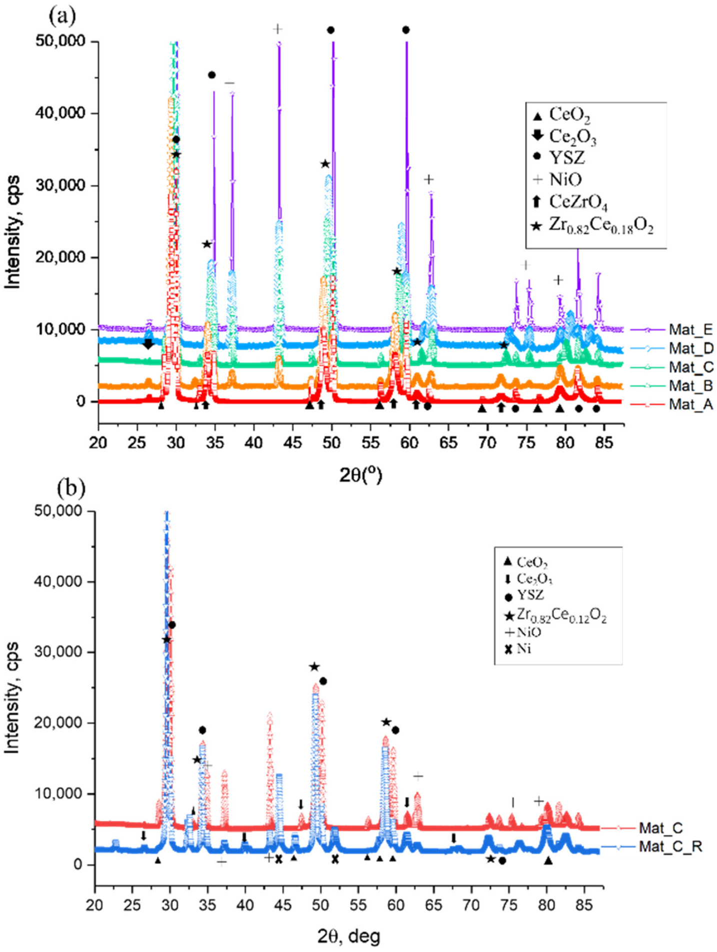

Figure 2. XRD results of ceramic DL-HFs for (**a**) Mat_A to Mat_E, (**b**) unreduced Mat_C and reduced Mat_C.

It is interesting to note that two types of ceria–zirconia phases were detected in each Mat_A, Mat_B, Mat_C and Mat_D, which are $CeZrO_4$ and $Zr_{0.82}Ce_{0.12}O_2$. The $CeZrO_4$ found in Mat_A and Mat_B contain higher molar ratios of Ce compared to $Zr_{0.82}Ce_{0.12}O_2$ found in Mat_C and Mat_D. Mat_A to Mat_C were also found to contain minority peaks of Ce(III) in the form of Ce_2O_3, as found by the database search. Such event was observed in a few studies, where sintering of CeO_2 at short lengths of time tends to cause low oxygen content in the ceria compound, where the oxide from the CeO_2 escaped, leaving more oxygen-deficient Ce_2O_3 behind [18]. The presence of Zr is also known to create the Ce(IV)/Ce(III) pair in the CeO_2 compound [19]. The database search also indicates that the Y_2O_3 phase was present, showing the leaching of Y_2O_3 out of the YSZ phase. Since the ceria–zirconia phase was also detected, this result might suggest that the CeO_2 has replaced the yttria in the YSZ material, which is also observed in other studies [20].

Two regions of interest are shown in Table 2. The region at 2θ of 47.5° corresponds to phase (2 0 2) of CeO_2, while 50.2° corresponds to the (2 0 2) of ZrO_2 in the YSZ used. Intermediate peaks found between these two peaks are 48.2° and 48.5°, corresponding to the phase (4 4 0) and (1 1 2) of $CeZrO_4$ and $Zr_{0.82}Ce_{0.12}O_2$ each. Thus, when the amount of CeO_2 increases in a mixture of CeO_2 and YSZ, sintering will produce a $Ce_xZr_{1-x}O_2$ phase with a large x value, increasing the d-spacing in the process. A similar trend can be seen in 2θ of 56.3° and 59.6°. No insertion of NiO into the ZrO_2 or CeO_2 was found in any sample. This shows that, in the presence of the NiO–CeO_2–ZrO_2 system, the interacting materials are only between CeO_2 and ZrO_2, which made the system behave equally to CeO_2–ZrO_2.

Table 2. Selected region showing changing of d-spacing as zirconia mixed with CeO_2 from Mat_A to Mat_E.

2θ, °	d-Spacing, A	Plane	Compound	DL-HF
47.5	1.9131	202	CeO_2	Mat_A, Mat_B, Mat_C
48.2	1.8640	440	$CeZrO_4$	Mat_A, Mat_B
49.5	1.8373	112	$Zr_{0.82}Ce_{0.18}O_2$	Mat_C, Mat_D
50.2	1.8151	202	ZrO_2 in $((ZrO_2)_{0.88}(Y_2O_3)_{0.12})_{0.893}$	All
56.3	1.6315	311	CeO_2	Mat_A, Mat_C
58.0	1.5896	622	$CeZrO_4$	Mat_A, Mat_B
58.5	1.5759	013	$Zr_{0.82}Ce_{0.18}O_2$	Mat_C, Mat_D
59.6	1.5491	311	ZrO_2 in $((ZrO_2)_{0.88}(Y_2O_3)_{0.12})_{0.893}$	All

XRD results of Mat_C and reduced Mat_C are shown in Figure 2b. Only results of Mat_C are shown here as it contains similar amounts of NiO and CeO_2, and it can be used to represent the result of other SOFC since it contains all the ceria–zirconia species present in Mat_A and Mat_E. Upon reduction with H_2 gas, Mat_C produced Ni metal together with decreasing peaks of CeO_2 and increased peaks of Ce_2O_3. The increased amount shows that not only the NiO reduction occurred but the reduction of Ce(IV) to Ce(III) also took place in the sample. This phenomenon is well-known to occur in the operation of CeO_2 in a highly reducing environment, where the usage of electrolytes is unfavorable to the n-type conductivity gained in the Ce(IV)–Ce(III) mixture [21]. However, the existence of the Ce(IV)–Ce(III) mixture was suggested by few studies to actually have higher catalytic activity towards oxidizing hydrocarbon compared to Ce(IV) alone [22,23]. The increased electronic conduction and different oxidation state might give more electron and oxide ion mobility to the mixture, causing it to perform a better oxidation reaction.

Figure 3 shows the results for the mechanical testing. The bending strength is shown in Figure 3a for Mat_A to Mat_E from sintering temperatures of 1350 to 1550 °C. This temperature range was chosen based on the optimal sintering temperature of CeO_2 and YSZ [24,25]. The bending strength of Mat_A was shown to be the highest in all temperature ranges compared to the other DL-HF.

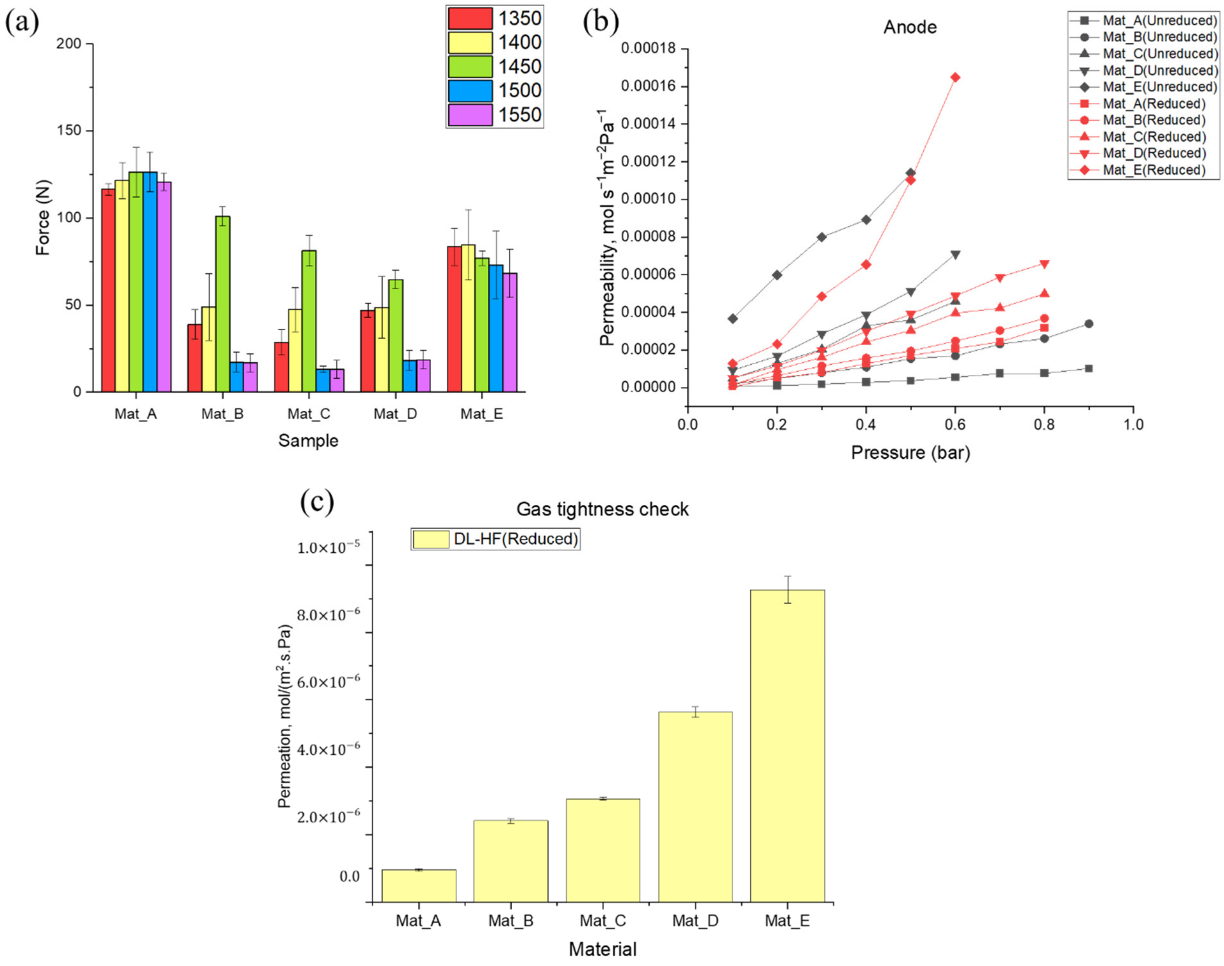

Figure 3. Sub-figure (**a**) shows the mechanical strength measured through bending strength of ceramic DL-HF from Mat_A to Mat_E at sintering temperatures from 1350 to 1450 °C (sample number = 3), (**b**) shows the gas rate of gas permeation through the anode and (**c**) gas tightness of the electrolyte layer.

The bending strength of Mat_A reached the optimal point at sintering temperatures from 1450 to 1500 °C before declining, while the bending strength of Mat_B, Mat_C and Mat_D achieved optimal strength at a temperature of 1450 °C before significantly dropping at 1500 °C. Mat_E achieved optimal bending strength at 1400 °C, before declining slowly. Mat_E with 50% NiO–50% YSZ, nonetheless, has relatively similar bending strength from 1350 to 1550 °C, which is expected since YSZ is known to exhibit almost similar density over 1350 °C sintering temperature [25]. The rate of shrinkage of YSZ also increases as the sintering temperature increases, which might further explain this observation [25].

Mat_A (50% CeO_2, 50% YSZ) was found to achieve optimal strength at a slightly higher temperature compared to Mat_E (50% NiO, 50% YSZ). From an XRD perspective, the diffusion of CeO_2 into the ZrO_2 lattice producing the ceria–zirconia compound was found to produce a ceramic with a higher strength compared to YSZ alone in Mat_A (no diffusion of NiO was observed).

Low mechanical strength in the mixture of the CeO_2–Ni anode (Mat_B, Mat_C, Mat_D) was observed at all temperatures. At the low temperature of 1350 °C, mechanical strength decreases from Mat_A to Mat_C and increases back to Mat_E. For sintering temperatures from 1350 to 1550 °C, the lowest mechanical strengths are all in Mat_C. The low mechanical strength may possibly be attributed to the presence of different types of ceria–zirconia compounds found in this membrane (and also in Mat_B and Mat_D) compared to Mat_A. Since Mat_E did not have these $Zr_{0.82}Ce_{0.12}O_2$ compounds, it is possible that the compound actually reduces the mechanical strength of the ceramic DL-HF. The same trend was also found in Mat_D, as this sample contains these $Zr_{0.82}Ce_{0.12}O_2$ compounds as well. Higher mechanical strength in Mat_A compared to Mat_E, however, indicates that $CeZrO_4$ actually gives larger mechanical strength. The authors of [24] noted that the increase in gadolinium-doped ceria (GDC) content in YSZ induces the shift in oxide peak plane in the XRD content, signifying possible dissolution of CeO_2 into the ZrO_2 [26]. The dissolution may create a denser CeO_2–ZrO_2 structure as compared to YSZ [20]. A study on the GDC–YSZ system shows that as the YSZ component increases, even though the coefficient of thermal expansion (CTE) increases, the chemical expansion is actually higher in the GDC–YSZ mixture compared to GDC or YSZ alone [27]. NiO–YSZ was shown to have a CTE from 10.3×10^{-6} (pure YSZ) to less than 14×10^{-6} K^{-1} (60% NiO:40% YSZ) [28], which is different from the CTE from 13.2×10^{-6} to 14.7×10^{-6} K^{-1} in the ceria–zirconia system [29]. Low mechanical strength experienced in the mixture might be the result of the CTE mismatch between ceria–zirconia species and NiO–YSZ material.

Gas permeability across the anode is given in Figure 3b. Gas permeability is the lowest in Mat_A and increased from Mat_A to Mat_E. This property suggests that the higher the CeO_2 content, the lesser the gas permeation. As observed in Figure 1ii, the low permeability is also caused by the lesser presence of finger-like formations in the anode of ceramic DL-HF [30]. The lower gas permeability in higher CeO_2 content combined with the higher mechanical strength observed from Mat_C to Mat_A signifies that the presence of CeO_2 or ceria–zirconia does not only yield a harder anode but also a less porous one. This might be explained by the smaller finger-like projection and more sponge-like porous structure obtained from Mat_E to Mat_A, as observed in Figure 1ii. The lack of a large porous structure in Mat_A resulted in lower gas permeability. Furthermore, at sintering temperatures above 1350 °C, the rate of shrinkage in YSZ is larger than the rate of shrinkage in the ceria–zirconia structure [31].

Gas permeability was found to increase after reduction by H_2 gas. This is expected as when the NiO was reduced to Ni, volume shrinkage occurred, causing enlargement of pores and hence higher gas permeation. However, it is also to be noted that even though Mat_A contains no NiO, reduction elevates the gas permeability as well. This is caused by a reduction of Ce(IV) to Ce(III) or from CeO_2 to Ce_2O_3, as observed in XRD, which similarly leads to volume shrinkage and higher gas permeation. Similar trends of gas permeability are also observed in the gas tightness test, as shown in Figure 3c. We expect that the explanation of the behavior of the gas tightness check of the electrolyte is similar to the gas permeation in the anode. Since the thickness of the electrolyte was the same in all samples, the gas tightness of the electrolyte was found to be affected by the gas permeation rate through the anode in this study.

The anode conductivity obtained is shown in Figure 4. The conductivity of the Ni-containing anode shows percolation was achieved at above 30% Ni by volume, which is Mat_E (50% NiO by weight). Lowering the content of NiO to below 50% NiO will lead the conductivity to drop by a magnitude of six, as observed in Mat_D. This is similarly reported in early studies [32]. It is important to note that the conductivity obtained was lower than that reported in the literature, which is due to different methodologies. The conductivity, as reported in other studies, was measured by pressuring the sharp probe onto the anode surface and is only applicable since the geometry of the SOFC is planar. Here, the same methodology cannot be used due to the tubular geometry, and less pressure is able to be applied to the lumen of the tubular SOFC. Nonetheless, a large jump in conductivities is observed as in other studies, showing the good reliability of our method.

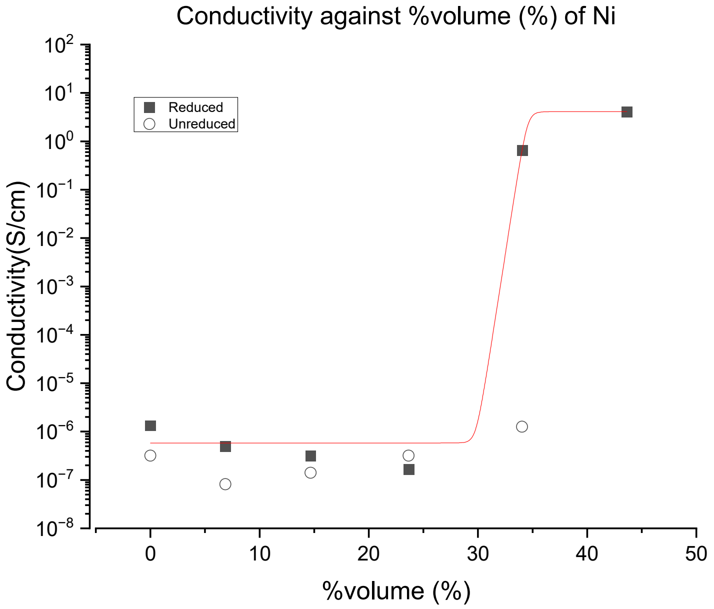

Figure 4. Conductivity of the anode before and after reduction by H_2 gas.

Anode conductivity is crucial in the performance of SOFC, and low anode conductivity has been shown to correlate with lower performance. Low conductivity is expected in this study due to the low content of Ni. However, since Ni is also known to cause coking, a negative effect of lowering the Ni content was offset with the addition of CeO_2, which was known to provide conductivity upon reduction. It is interesting to note that the conductivity of Mat_A is slightly higher than the conductivity of Mat_B. A similar trend was also observed in the GDC–YSZ system, where it was found that the conductivity of pure GDC and YSZ is higher than the mixture of GDC–YSZ [20]. Another explanation for the higher conductivity is possibly due to the denser packing structure in Mat_A compared to Mat_B, as shown in the SEM imaging in Figure 1. A denser structure allows for a better conductance path of electrons and hence higher conductivity [33].

3.2. Fuel Cell Performance

Fuel cell performance testing was performed at 700, 750, 800, 850 and 900 °C. The temperature of 700 °C was selected as the lowest temperature for testing since the YSZ electrolyte was found to have lower performance below this point [2]. High operating temperatures are expected to yield better performance for SOFC operating in hydrocarbon fuel since higher temperature ensures operation in the hydrocarbon reforming area [34]. Nonetheless, in this setup, we would like to test the effect of CeO_2 as an oxidizing catalyst in SOFC without depending much on the reforming process; thus, 900 °C was selected as the highest operating temperature to be tested.

3.2.1. Power Density Analysis (I-V Diagram)

The current–voltage (I-V) diagram and power measurements are given in Figures A5 and A6, and Electrochemical Impedance Spectroscopy (EIS) is given in Figures A7 and A8 in Appendix A for each H_2 and CH_4 fuel.

For I-V measurements, generally, when run in H_2 fuel, the MPD increased as the operating temperature increased, which is typical in YSZ-type cells for this operating temperature range. The MPD for SOFC running on H_2 and CH_4 is summarized in Figure 5. The MPD was found to unexpectedly drop from Mat_A to Mat_B and rise back again from Mat_B to Mat_E. The increment observed from Mat_B to Mat_E signifies that Ni presence is crucial in SOFC operating in H_2 fuel, in which it acts as a catalyst and conductor. Nonetheless, Mat_A was found to have a higher MPD than Mat_B despite having no Ni content at all. The low catalytic activity of CeO_2 in oxidizing H_2 was well understood and explained by Density Functional Theory (DFT) modeling, which was shown to be inferior compared to Ni [35]. Therefore, this high MPD might be possibly explained by the presence of Ce(III) and possibly the ceria–zirconia compound as well, where both were shown to be able to function as an oxidation catalyst [36,37]. Apart from that, the presence of a large amount of CeO_2 in Mat_A compared to Mat_B might yield more Ce(IV)–Ce(III), increasing the anode conductivity and giving a slightly better performance [21]. This slightly higher conductivity can be observed in Figure 4.

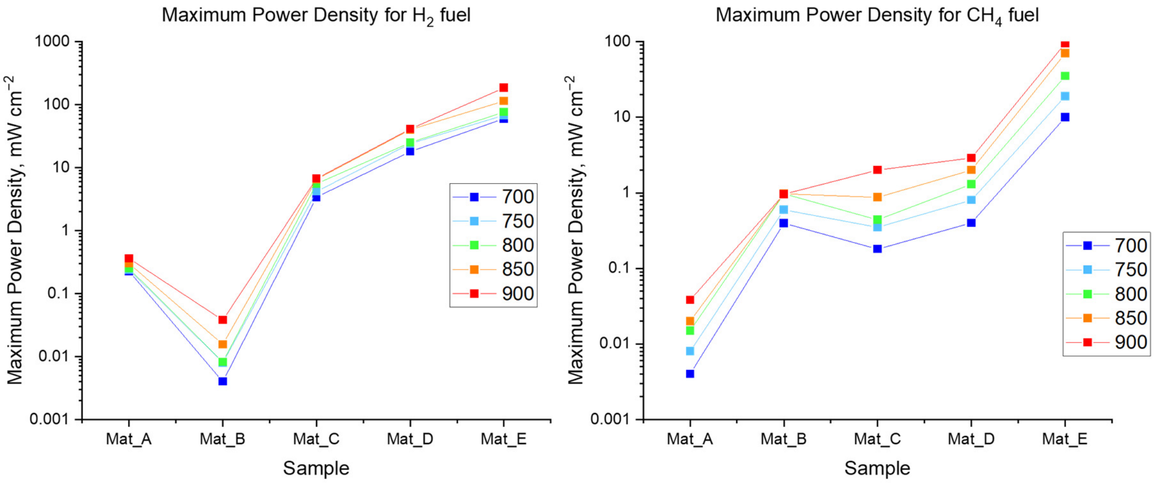

(**a**) (**b**)

Figure 5. (**a**) MPD for H_2 fuel and (**b**) MPD for CH_4 fuel.

It is interesting to note that even though Mat_D has conductivity below the threshold value, the MPD values of Mat_D (41 and 2.9 mW cm^{-2} at 900 °C in H_2 and CH_4 each) are relatively near to that of Mat_E (185 and 95 mW cm^{-2} at 900 °C in H_2 and CH_4 each) compared to that of Mat_C (6.7 and 2.0 mW cm^{-2} at 900 °C in H_2 and CH_4 each). Since Mat_D contains 12.5% less NiO content than Mat_E, Mat_D can be considered as a promising low-nickel-content anode to be used.

3.2.2. Electrochemical Impedance Spectroscopy (EIS)

When run on hydrogen fuel, generally the impedance for all of the samples decreases as the temperature increase. This is a typical characteristic of ohmic resistance due to resistance towards oxide ion movement through the electrolyte [20]. As ionic conductivity of YSZ increases as the temperature increases, the ohmic resistance drops as the operating temperature increases, as ionic conductivity is a temperature-activated process [38].

The impedance spectroscopy also shows characteristics of gas transfer limitations in SOFC with higher CeO_2 content (Mat_A to Mat_C). This is observed with an increasing value of impedance at low frequency with the characteristic of 45^o inclination, described as the Warburg process [39]. However, in Mat_A to Mat_C, the peak at low frequency started to form a loop at higher temperatures, suggesting the reduction in gas transfer resistance. Another characteristic is that the impedance seems to consist of two loops that converge to form one loop at higher temperatures. As shown in Figure A9 in Appendix A, the first loop is often described as the polarization resistance, (R_{ct}), associated with the accumulation of charge at the electrode due to the difficulty of charge transfer to reactants. It is also associated with the resistance towards the transfer of the electron from the cathode surface to the oxygen, or transfer of electron from the oxide ion to the anode, which occurs due to the catalytic limitation of the electrode. The second loop is often called concentration polarization, R_{conc} resistance, which occurs due to mass transport limitation in the electrode associated with morphology of the electrode [39].

The value of R_{ohm} for each EIS was measured and plotted according to temperatures, and subsequently, an Arrhenius plot was prepared from the data to obtain the activation energy, E_a, for the ohmic process, as shown in Figure 6a,b,e,f. Similar data processing was applied to R_{ct} and is shown in Figure 6c,d,g,h. The activation energy, E_a, obtained for the ohmic process and charge transfer process is shown in Figure 7.

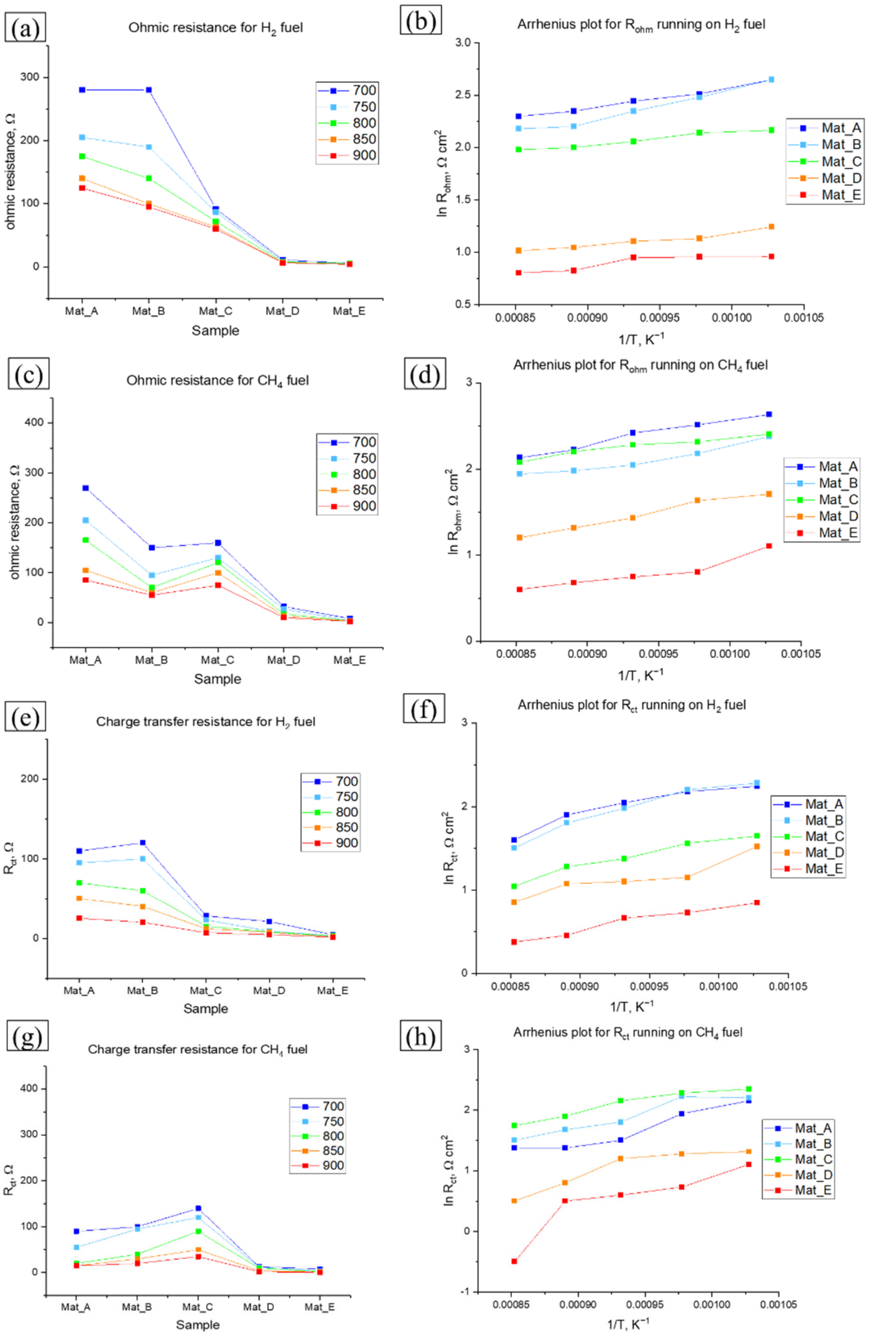

Figure 6. Ohmic resistance for H_2 (**a**) and CH_4 (**c**) and charge transfer resistance for H_2 (**e**) and CH_4 (**g**). Arrhenius plot for ohmic resistance for H_2 (**b**) and CH_4 (**d**), and Arrhenius plot for charge transfer resistance for H_2 (**f**) and CH_4 (**h**).

3.2.3. R_{ohm} for Operation in H_2 and CH_4

The R_{ohm} value was found to decrease as the Ni content increased from Mat_A to Mat_E in both H_2 and CH_4 fuel. The ohmic resistance is understood to be the process involving the movement of O^{2-} ions across the cathode, electrolyte and anode, where a lower R_{ohm} is favored for a higher MPD of the cell [20]. This is reflected in the reading of MPD shown in Figure 5. For all SOFC, R_{ohm} decreases as temperature increases, showing typical temperature-activated processes of the O^{2-} movement. The trend in R_{ohm} follows exactly the trend seen in conductivity, where higher conductivity was found to yield lower R_{ohm}, despite having similar content of YSZ in the cathode, electrolyte and anode. This shows that anode conductivity plays a crucial role in R_{ohm}. Anode conductivity may have made it easier for the electron to move through the anode. The oxidation of O^{2-} at the anode might have been impeded if the anode conductivity was low simply because the electron cannot leave O^{2-} or the oxidation reaction because there is no conduction path, leaving the O^{2-} transport impeded as well [40].

It is interesting to note that even though Mat_D has conductivity below a threshold value, the R_{ohm} values of Mat_D (6.5 and 10.0 Ω cm^2 at 900 °C in H_2 and CH_4 each) are relatively near to that of Mat_E (4.0 and 2.5 Ω cm^2 at 900 °C in H_2 and CH_4 each) compared to that of Mat_C (60.1 and 70.2 Ω cm^2 at 900 °C in H_2 and CH_4 each). Since Mat_D contains 12.5% less NiO content than Mat_E, Mat_D can be considered as a promising low-nickel-content anode to be used.

3.2.4. R_{ct} for Operation in H_2 and CH_4

R_{ct} involves the transfer of charge where oxygen is reduced at the cathode or the fuel is oxidized at the anode [31]. However, since the cathode thickness is the same for all of the SOFCs, the value of R_{ct} here reflects the oxidation of fuel at the anode.

R_{ct} was found to be lower as Ni content increased in H_2. This is expected since the oxidation of H_2 is catalyzed by the Ni metal, hence increasing the Ni content resulted in lower R_{ct} values. The trend is actually similar to the trend of anode conductivity as well. As explained in the R_{ohm} section, there might be another factor affecting the R_{ct} when operating in H_2, which is anode conductivity. Here, the high conductivity and high catalytic rate both led to the reduction of R_{ct} as the Ni content increased.

R_{ct} in CH_4, on the other hand, increased from Mat_A to Mat_C, then decreased rapidly to Mat_D and Mat_E. The charge transfer process in CH_4 oxidation is catalyzed both by Ni and at lower rates by CeO_2 [35]. However, as explained in the R_{ohm} section, R_{ct} may actually depend on the value of R_{ohm} and hence anode conductivity as well, since lower anode conductivity may make oxidation harder to proceed since the electron cannot leave the oxidation reaction [41]. With the lack of Ni (Mat_A and Mat_B), oxidation is catalyzed by CeO_2, but since the anode conductivity is low, the rate is lower, resulting in higher R_{ct}. In the presence of Ni (Mat_D and Mat_E), it can be achieved with Ni at a higher rate and, coupled with high conductivity, push the R_{ct} value even lower. We believe that the Mat_C mixture provided higher R_{ct}, possibly due to lesser catalytic activity due to less CeO_2 and Ni, coupled with a lower-than-threshold value of anode conductivity.

It needs to be noted that the anode composition of Mat_D has almost similar Rct (4.5 and 1.9 Ω cm^2 at 900 °C in H_2 and CH_4 each) to Mat_E (1.5 and 0.2 Ω cm^2 at 900 °C in H_2 and CH_4 each) compared to Mat_C (7.2 and 34.9 Ω cm^2 at 900 °C in H_2 and CH_4 each), showing 37.5% Ni, 12.5% CeO_2 and 50% YSZ to be the suitable low-Ni anode for use.

3.2.5. E_a for R_{ohm} for Operation in H_2 and CH_4

The value of E_a for R_{ohm} shows the energy barrier for the ohmic process or the resistance towards the flow of oxide ions in the electrolyte [14,20]. Greater changes in R_{ohm} that result from changes in temperature yield higher E_a, signifying that higher temperature will supply more energy for the reactant to overcome the energy barrier. In the case of R_{ohm}, higher E_a indicates a higher energy barrier for ionic transportation of mainly the O^{2-} ion to move through the electrolyte. Higher E_a is undesirable since the process usually requires a high operating temperature.

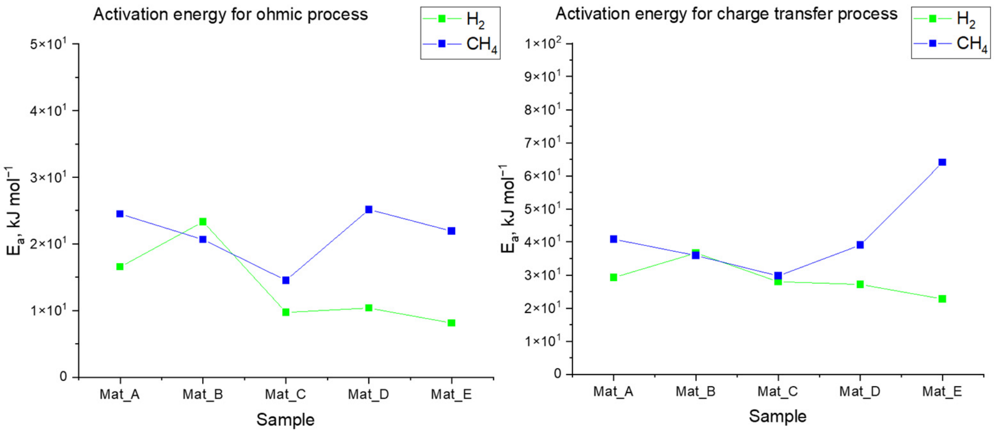

Figure 7. E_a for ohmic resistance and charge transfer process for H_2 and CH_4.

The value of E_a for R_{ohm} and R_{ct} for each H_2 and CH_4 is shown in Figure 7. Briefly, the E_a for R_{ohm} for H_2 was found to be 16.5, 23.3, 9.7, 10.3 and 8.1 kJ mol^{-1} for Mat_A, Mat_B, Mat_C, Mat_D and Mat_E. E_a for R_{ohm} for operation in H_2 generally follows the same trendline as in conductivity, where Mat_A is lower than Mat_B but becomes lower as the composition approaches Mat_E. A possible explanation for this observation is that movement of the oxide ion through the electrolyte is a multistep process, which partly consists of the process of electron transport movement, as illustrated in Figure 8a,b. For example, for the O^{2-} ion to move, O^{2-} production via reduction at the cathode and O^{2-} oxidation at the anode involves the transfer of an electron from and to the oxygen, and thus, should the flow of electron be resisted at the anode (or cathode), the flow of oxide ions will also be affected across the electrolyte [20].

The E_a for H_2 R_{ohm} is also generally lower than for CH_4 (except for Mat_B), showing the effect of fuel on the resistance to O^{2-} movement. This is known since the presence of H_2 in a CeO_2-containing anode is known to reduce the CeO_2 to Ce_2O_3, which offers an alternate O^{2-} movement pathway other than through the YSZ, which has lower E_a. This increases the O^{2-} mobility and hence the flow of the O^{2-} ion [40]. However, in the operation in H_2, the anode conductivity seems to be the limiting factor in the R_{ohm}, while in CH_4, the anode conductivity is not the limiting factor [31].

The E_a for R_{ohm} for CH_4 was found to be 24.4, 20.6, 14.5, 25.1 and 21.9 kJ mol^{-1} for Mat_A, Mat_B, Mat_C, Mat_D and Mat_E. Compared to H_2, E_a for R_{ohm} for operation in CH_4, on the other hand, drops from Mat_A to Mat_B, increased to Mat_D and decreased slightly to Mat_E. The possible explanation for this phenomenon is similar to that of R_{ct} for H_2, where the movement of oxide ion is a multistep process consisting of an electron conduction process and O^{2-} ion generation process, etc., as shown in Figure 8c.

In a sample with high Ni content (Mat_D to Mat_E), the drop in E_a is actually the result of the increase in the anode conductivity, giving lower E_a for electron conductance and hence Rohm. The Ea for Mat_A to Mat_C also has a downward trend due to a similar effect. However, as the CeO_2 content decreases from Mat_A to Mat_E, the conductance of O^{2-} also decreases, giving a higher E_a. This can be observed in higher Ea in Mat_D and Mat_E compared to Mat_B and Mat_C. From Mat_A to Mat_C with low Ni content but with high CeO_2 content, the low E_a for R_{ohm} is actually caused by the presence of high amounts of CeO_2, Ce(IV)/Ce(III) pairs and ceria–zirconia compounds, which are known to be able to conduct O^{2-} [40].

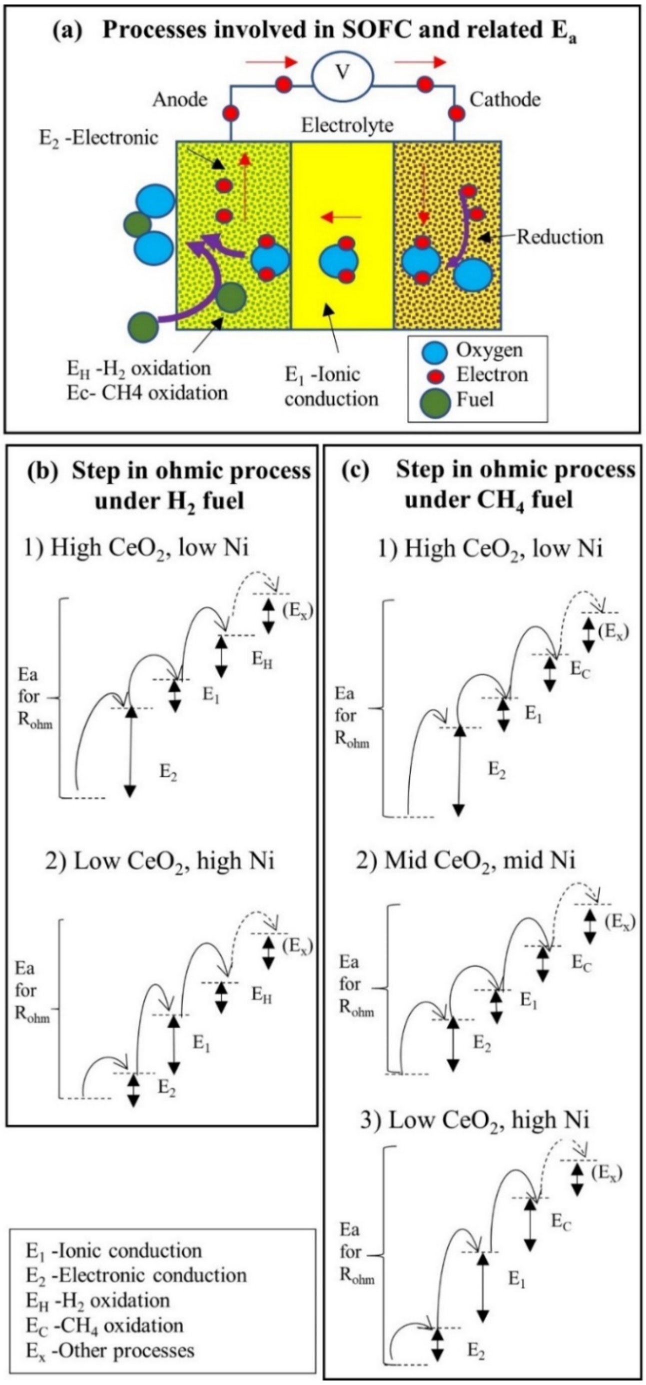

Figure 8. Illustration of processes involved in SOFC and related E_a.

3.2.6. E_a for R_{ct} for Operation in H_2

The E_a for R_{ct} for H_2 was found to be 29.2, 36.6, 27.9, 27.1 and 22.7 kJ mol^{-1} for each Mat_A, Mat_B, Mat_C, Mat_D and Mat_E. The trend of E_a for the charge transfer process in H_2 follows a similar pattern as R_{ohm} and anode conductivity. For H_2, E_a increases from Mat_A to Mat_B and decreases back to Mat_E, achieving a maximum at Mat_B. While the pattern suggests anode conductivity as the rate-limiting step, we believe that the charge transfer process of H_2 is also a multiple-step process, as shown in Figure 8b, but the other process has lower E_a than the electron conduction process. This is because the oxidation of H_2 may follow a different route depending on the content of ceria–zirconia, the Ce(IV)/Ce(III) pair and Ni [19]. Lowering the concentration of both CeO_2 or NiO (as in Mat_B to Mat_D) results in higher Ea. Both Ni and CeO_2 are known to be able to adsorb H_2

gas onto their surface, where the rate of adsorption of H_2 onto Ni is greater than the rate of adsorption on CeO_2 [42]. However, unlike Ni that requires ZrO_2 (in YSZ) to oxidize the adsorbed hydrogen, CeO_2 can oxidize the H_2 by directly turning it into Ce_2O_3. Thus, from Mat_A to Mat_B where the concentration of Ni is still too low to catalyze H_2 oxidation, the oxidation is performed by CeO_2, and the increment of E_a observed from Mat_A to Mat_B is the result of the lowering of CeO_2 content. However, in Mat_C to Mat_E, the presence of higher content of Ni led to a rapid reduction of E_a for R_{ct} of H_2. This effect is obvious in the charge transfer process of CH_4.

3.2.7. E_a for R_{ct} for Operation in CH_4

The E_a for R_{ct} for CH_4 was found to be 40.8, 35.9, 29.7, 39.0 and 64.0 kJ mol^{-1} for Mat_A, Mat_B, Mat_C, Mat_D and Mat_E. For oxidation of CH_4, the trend is the reverse of the trend seen in $H_{2,}$ where the E_a decreased from Mat_A to Mat_C and increased back to Mat_E. This trend is also almost similarly observed by [17], which found the presence of Ni on ceria–zirconia increased oxidation of methane [19]. The performance is high when small amounts of Zr are present in the Ni–ceria–zirconia compound, where the rate of methane oxidation was found to be $Ni–ZrO_2 < Ni–Ce_{0.17}Zr_{0.83}O_2 < Ni–CeO_2 < Ni–Ce_{0.83}Zr_{0.17}O_2$. Similarly, in our result, Mat_A containing CeO_2, $Ce_{0.5}Zr_{0.5}O_2$ and ZrO_2 (in YSZ) has higher E_a compared to Mat_C containing $Ni–CeO_2$, $Ni–Ce_{0.18}Zr_{0.82}O_2$ and $Ni–ZrO_2$ (in YSZ). Mat_E that contains only $Ni–ZrO_2$ (in YSZ) has the highest E_a for R_{ct}. This observation indicates that oxidation of CH_4 takes more energy if performed by Ni alone compared to ceria–zirconia alone. Oxidation of CH_4 in a mixture of $Ni–Ce_{1-x}Zr_xO_2$ takes different pathways that have lower E_a than on Ni or ceria–zirconia alone.

3.2.8. Comparison of Effects of Ni and CeO_2 Content on R_{ohm} and R_{ct} on H_2 and CH_4 Fuel

A summary of the effect of Ni and CeO_2 content on electronic conductivity, O^{2-} conductivity, H_2 oxidation and CH_4 oxidation was made based on observations from the I-V curve, MPD, EIS and E_a and is shown in Table 3. Also based on these observations, a summary of E_a for R_{ohm} and R_{ct} when operating in H_2 and CH_4 fuel is shown in Table 4.

Table 3. Effect of Ni and CeO_2 content on electronic conductivity, O^{2-} conductivity, H_2 oxidation and CH_4 oxidation.

Properties	**Low Ni** **High CeO_2**	**High Ni** **Low CeO_2**	**Remark**
Electronic Conductivity	Low Supplied by Ce(III)–Ce(IV)	High Supplied by Ni	
O^{2-} conductivity	High Aided by CeO_2	Low	
H_2 oxidation	Done by CeO_2–YSZ Lower rate	Done by Ni–YSZ High rate	Higher E_a for Ni–CeO_2–YSZ
CH_4 oxidation	Low	Low	Lower E_a in Ni–CeO_2–YSZ

Table 4. Conclusion for E_a for R_{ohm} and R_{ct} when operating in H_2 and CH_4.

Fuel	**E_a for R_{ohm}**	**E_a for R_{ct}**
H_2	Limited by anode conductivity Higher anode conductivity, lower E_a Anode conductivity is a rate-limiting step	Limited by anode conductivity Higher anode conductivity, lower E_a Anode conductivity is a rate-limiting step
CH_4	Limited by anode conductivity, oxide ion conductivity, fuel oxidation	Lower E_a for CH_4 oxidation observed in Ni–CeO_2–YSZ

Based on the anode conductivity reading, lowering the Ni content to lower than 50% NiO (Mat_E) in the anode was shown to produce a detrimental effect on the conductivity, where the anode conductivity drastically falls more than 10^7 times. However, based on the MPD value, large losses in the value were actually observed when the Ni content lowered to below 37.5% NiO (Mat_D), which sees the abrupt losses in MPD. Similarly, based on EIS data in H_2 and CH_4 fuel, a large value of impedance is observed in lower than 37.5% NiO. However, lowering of Ni coupled with an increasing amount of CeO_2 yield benefits in terms of reduction of E_a for R_{ct} for operation in CH_4, especially when the content of NiO–CeO_2–YSZ is balanced at 25%:25%:50% (Mat_C). Having relatively similar E_a for R_{ohm} for operation under H_2 and CH_4 with the lowest E_a for R_{ct} for CH_4, this anode content may be concluded to be the best to function as an anode for operation in CH_4. The property exhibited by Mat_C and Mat_D shows great potential in becoming a coking-tolerant anode for SOFC. Further study will be conducted to investigate the long-term performance of this anode in CH_4 fuel.

To date, there is no known study that fabricates CeO_2 directly into the Ni–YSZ anode of MT-SOFC via phase-inversion techniques as exhibited in this study, and hence no direct comparison of performance can be made. However, this study shows that it is possible to use low Ni content in an SOFC anode to limit the coking of an anode when used with hydrocarbon fuel in MT-SOFC. Low content Ni of 37.5% NiO with 12.5% CeO_2 (Mat_D) is shown here to obtain comparable performance with an anode containing 50% NiO (Mat_E) when compared in terms of MPD and impedance. MPD obtained by Mat_D is relatively low compared to traditional SOFC with 60% NiO and 40% YSZ but almost similar to another study that aims to reduce carbon deposition by using CeO_2 or ceria–zirconia anodes, as shown in Table 5.

Table 5. Comparison of MPD with other studies.

Anode	Geometry	Fuel	MPD, mW cm^{-2}	Source
37.5% NiO–12.5% CeO_2–50% YSZ	Micro-tubular	H_2	41	This work
37.5% NiO–12.5% CeO_2_50% YSZ	Micro-tubular	CH_4	2.9	This work
20% W–10% Ni–70% CeO_2	Planar	70% CH_4, 25% CO_2, 5% H_2	47.5	[43]
50% Ni–50% $Ce_{0.5}Zr_{0.5}O_2$	Planar	C_8H_{18}	80	[44]
42% Cu–CeO_2		CH_4 + H_2	55	[45]

It is important to note that the value of MPD may be low due to different fuel mixes used since this study uses pure CH_4 while other studies used mixtures of CH_4, H_2 and CO_2. The later fuel mixture indicates the reforming process in other studies. Furthermore, other studies use mainly planar geometry, which involves more preparation steps and more costs compared to the micro-tubular geometry in this study. The low MPD value is also caused by the thin electrolyte (~20 µm) used in this study that led to low gas tightness [14]. Low gas tightness may lead to leakage of oxygen from the cathode into the anode and fuel into the cathode, leading to the oxidation of fuel at the cathode and the reduction in oxygen in the anode, reducing the power output.

The low MPD problem in this SOFC can be mitigated by fabricating a thicker electrolyte to enhance the gas tightness. It can also be mitigated with a parallel stacking of MT-SOFC to increase current production or stacking in series to increase the voltage of the power sources if the MT-SOFC is to be commercialized [13]. Given the ease of fabrication and the smaller size of MT-SOFC compared to planar SOFC, the study provides great insight into fabricating low-nickel coking-tolerant SOFC. Furthermore, this type of SOFC can be used with renewable energy sources that contain hydrocarbon, such as biogas, or to extract energy from methane-based energy storage technology to ensure the most environmentally friendly application possible [46,47].

4. Conclusions

From this study, we found that lowering the Ni content to lower than 50% NiO (Mat_E) in the anode caused conductivity to drop by a magnitude of six, below the conductivity percolation threshold. However, the effect of anode conductivity on the MPD and EIS reading is only prominent when it reaches below 37.5% NiO. MPD for low Ni content, which are Mat_A, Mat_B and Mat_C (0% to 25% NiO), is generally low, while MPD for

Mat_D and Mat_E (37.5% to 50% NiO) is high. In terms of E_a for R_{ct} (which shows the catalytic properties of anodes), Ea are low for Mat_A to Mat_D compared to Mat_E. This resulted in Mat_D (37.5% NiO, 12.5% CeO_2) showing the lowest amount of Ni without abrupt negative effect on the MPD and impedance. Nonetheless, Mat_C was found to have the lowest E_a for R_{ct} for operation in CH_4, making it the best content to oxidize CH_4, but at a low MPD value.

By using Ea for Rohm and Rct as a method for investigation, we found a few differences between the oxidation of H_2 and CH_4 in the Ni–CeO_2–YSZ anode. They are:

1. In H_2 operation, E_a for R_{ohm} and R_{ct} is limited by anode conductivity, where higher anode conductivity will provide lower E_a. This implies that anode conductivity is a rate-limiting step in H_2 operation.
2. In CH_4 operation, E_a for R_{ohm} is limited by anode conductivity, oxide ion conductivity and fuel oxidation rate.
3. In CH_4 operation, lower E_a for R_{ct} or CH_4 oxidation is observed in the Ni–CeO_2–YSZ anode. The presence of Ni in ceria–zirconia increases the oxidation of methane.

Thus, based on this study, anode compositions containing 25% NiO:25% CeO_2:50% YSZ (Mat_C) and 37.5% NiO:12.5% CeO_2:50% YSZ (Mat_D) show promising results in becoming the low-Ni anode for coking-tolerant SOFC operation under CH_4 fuel.

Author Contributions: Conceptualization, H.A.S.; methodology, H.A.S.; software, H.A.S. and S.N.F.M.R.; validation, S.D. and M.A.R. (Mazlinda Ab Rahman); formal analysis, H.A.S. and S.N.F.M.R.; investigation, H.A.S., S.D. and M.A.R. (Mazlinda Ab Rahman); resources, H.A.S.; data curation, H.A.S. and S.N.F.M.R.; writing—original draft preparation, H.A.S. and S.N.F.M.R.; writing—review and editing, M.H.D.O., S.M.J., T.A.K., T.L., S.A.B. and N.O.; visualization, H.A.S. and S.N.F.M.R.; supervision, M.H.D.O. and S.M.J.; project administration, M.H.D.O.; funding acquisition, M.H.D.O., J.J., M.A.R. (Mukhlis A Rahman) and A.F.I. All authors have read and agreed to the published version of the manuscript.

Funding: The authors gratefully acknowledge the financial support from the Ministry of Higher Education Malaysia under the Fundamental Research Grant Scheme (FRGS) (Project Number: R.J130000.7809.5F161) and Malaysia Research University Network (MRUN) Grant (Project number: R.J130000.7809.4L867), and also Universiti Teknologi Malaysia under the UTM-UiTM SOFC Research Collaboration Grant (Project number: R.J130000.7309.4B676), Matching Grant (Project number: Q.J130000.3009.03M23) and UTM Zamalah Scholarship.

Institutional Review Board Statement: Not applicable.

Informed Consent Statement: Not applicable.

Data Availability Statement: The data presented in this study are available in Figures A5–A8 in Appendix A.

Conflicts of Interest: The authors declare no conflict of interest.

Appendix A

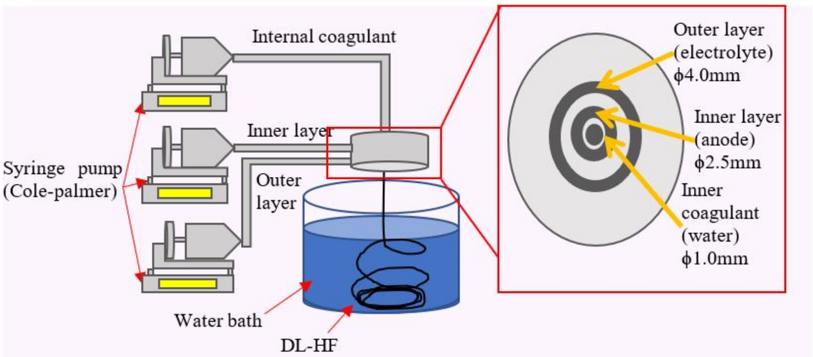

Figure A1. Setup for DL-HF co-extrusion, phase inversion process.

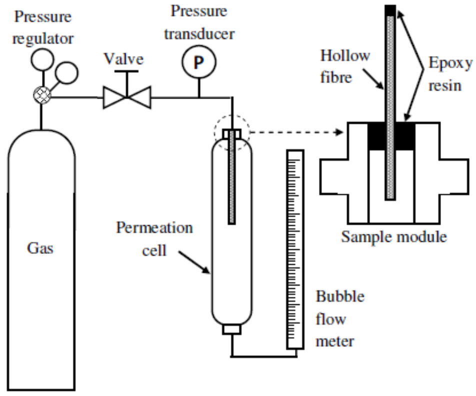

Figure A2. Gas permeation setup.

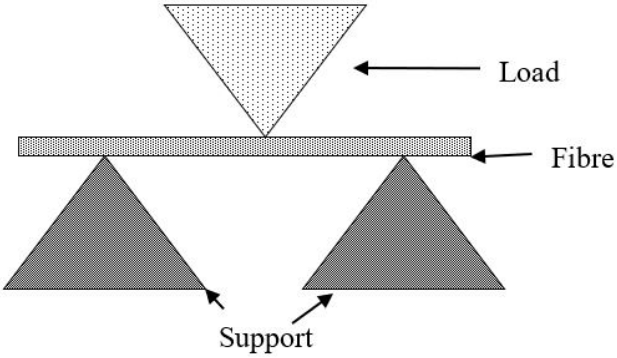

Figure A3. Schematic of the triple point bending test.

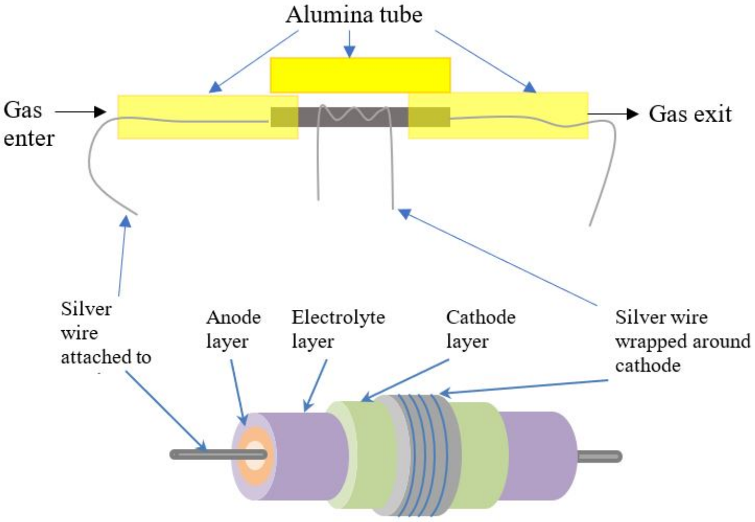

Figure A4. Illustration and image of setup for performance testing.

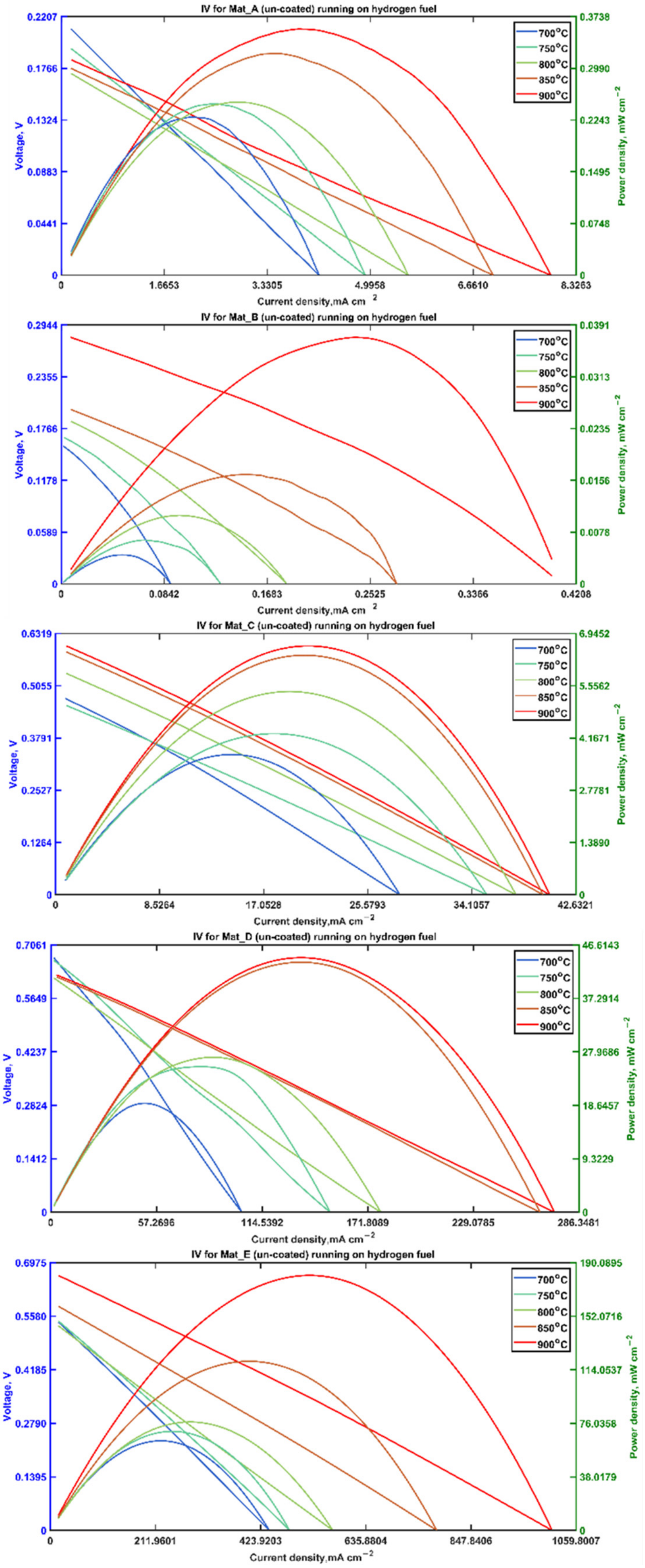

(i) Mat_A

(ii) Mat_B

(iii) Mat_C

(iv) Mat_D

(v) Mat_E

Figure A5. I-V and power measurement for Mat_A to Mat_E from temperatures 700 to 900 °C running in H_2 gas at 10 mL min^{-1}.

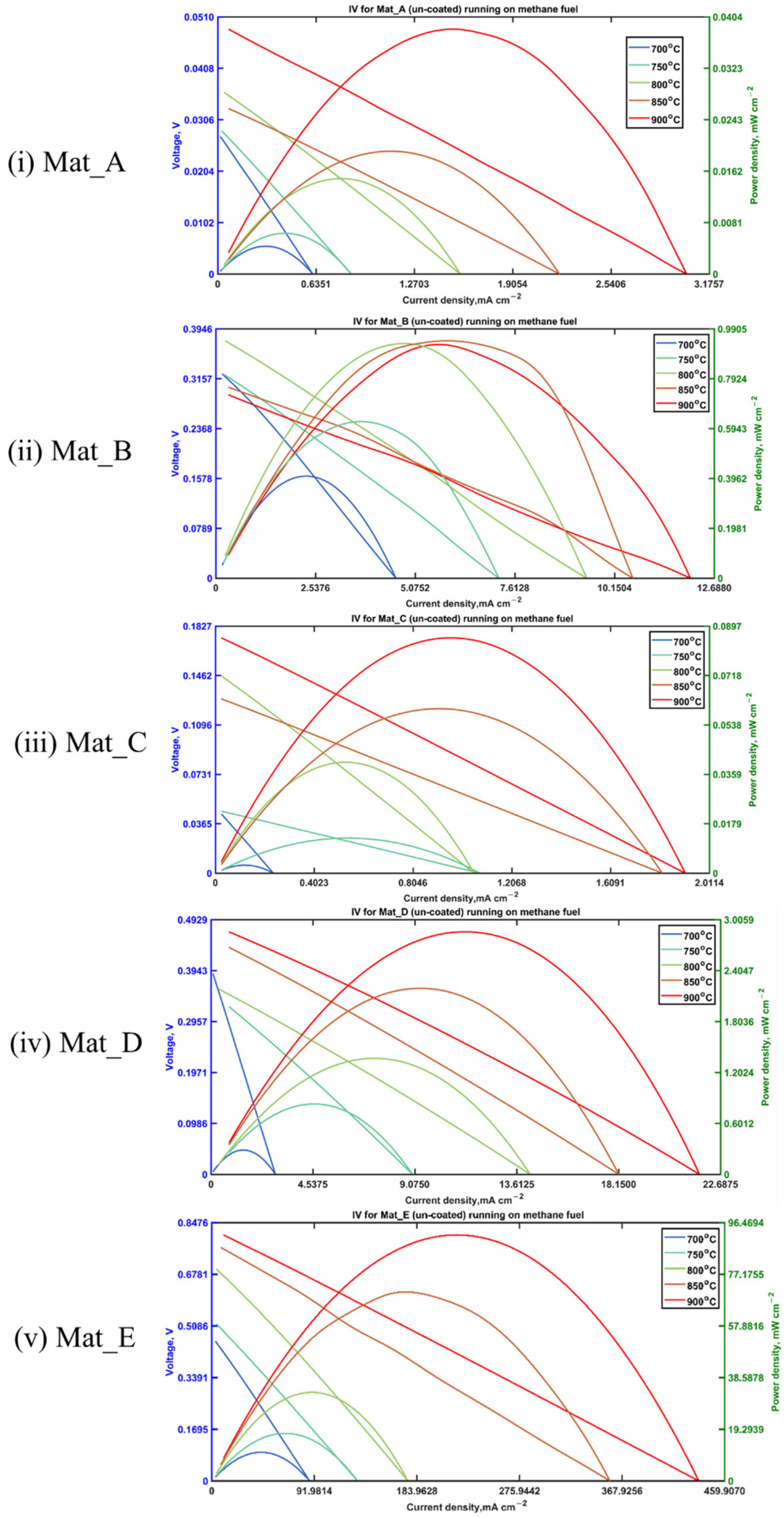

Figure A6. I-V and power measurement for Mat_A to Mat_E from temperatures 700 to 900 °C running in CH_4 at 10 mL min^{-1}.

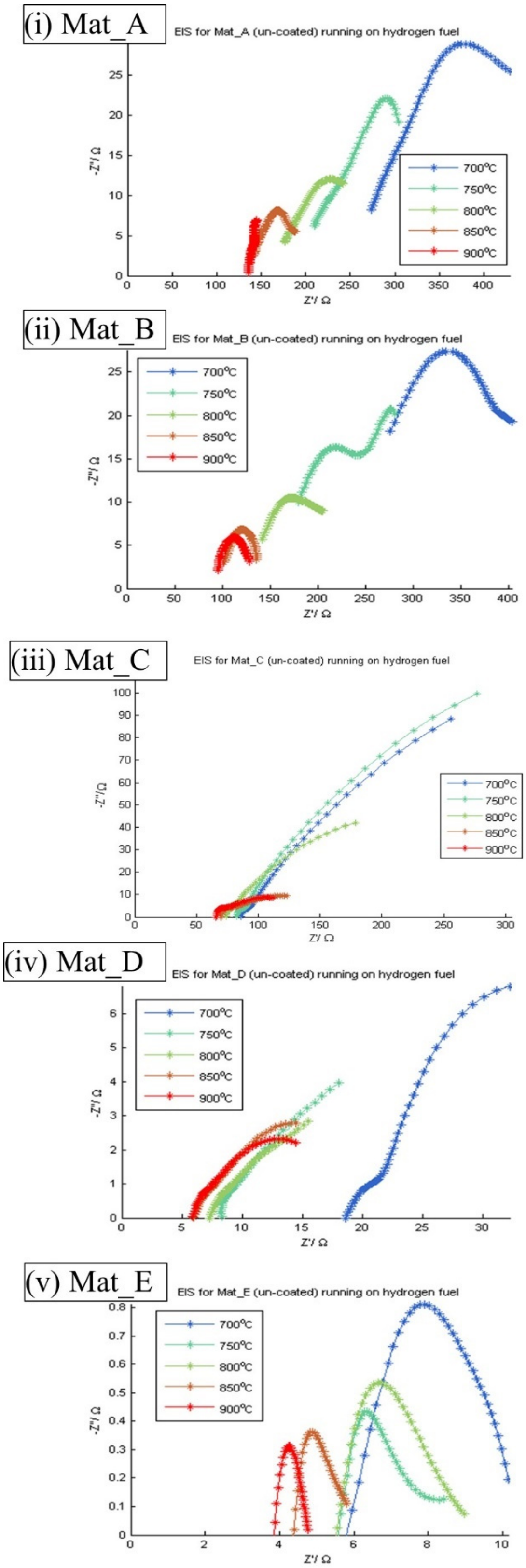

Figure A7. EIS for Mat_A to Mat_E from temperatures 700 to 900 °C running in H_2 gas at 10 mL min^{-1}.

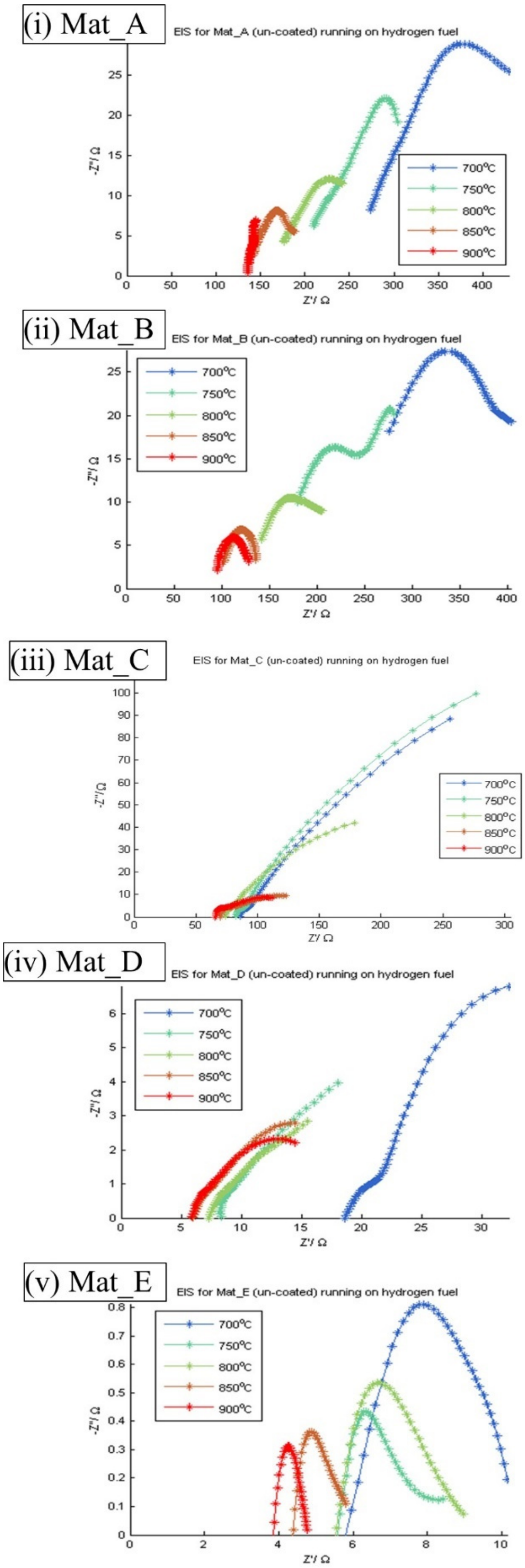

Figure A8. EIS for Mat_A to Mat_E from temperatures 700 to 900 °C running in CH_4 gas at 10 mL min^{-1}.

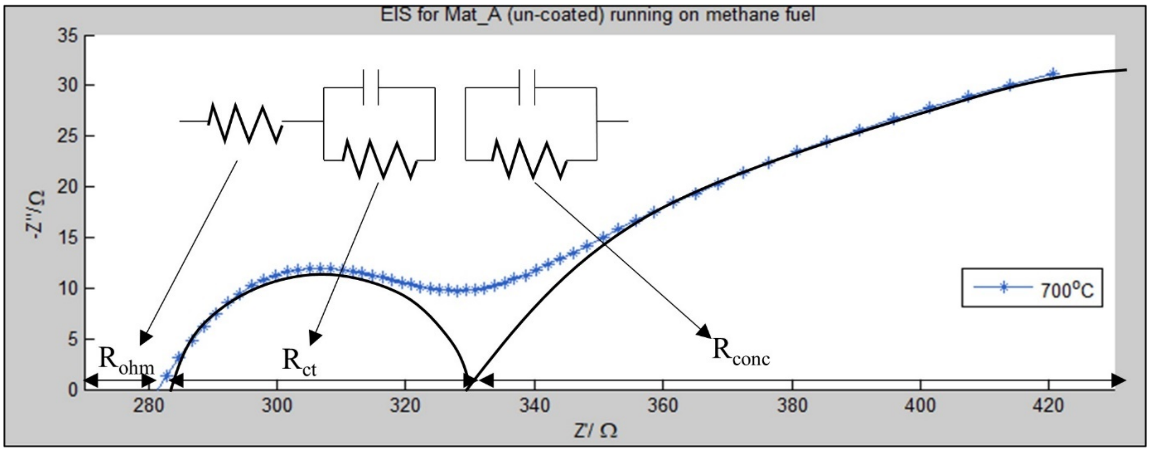

Figure A9. Equivalent circuit and measurement of R_{ohm} and R_{ct}.

References

1. Ades, M.; Adler, R.; Allan, R.; Anderson, J.; Argüez, A.; Arosio, C.; Augustine, J.A.; Azorin-Molina, C.; Barichivich, J.; Barnes, J.; et al. Global Climate. *Bull. Am. Meteorol. Soc.* **2020**, *101*, S9–S128. [CrossRef]
2. Shabri, H.A.; Othman, M.H.D.; Mohamed, M.A.; Kurniawan, T.A.; Jamil, S.M. Recent progress in metal-ceramic anode of solid oxide fuel cell for direct hydrocarbon fuel utilization: A review. *Fuel Process. Technol.* **2021**, *212*, 106626. [CrossRef]
3. Ahmed, S.; Aitani, A.; Rahman, F.; Al-Dawood, A.; Al-Muhaish, F. Decomposition of hydrocarbons to hydrogen and carbon. *Appl. Catal. A Gen.* **2009**, *359*, 1–24. [CrossRef]
4. Lee, J.; Theis, J.R.; Kyriakidou, E.A. Vehicle emissions trapping materials: Successes, challenges, and the path forward. *Appl. Catal. B Environ.* **2019**, *243*, 397–414. [CrossRef]
5. Hartvigsen, J.; Elangovan, S.; Elwell, J.; Larsen, D. Oxygen Production from Mars Atmosphere Carbon Dioxide Using Solid Oxide Electrolysis. *ECS Trans.* **2017**, *78*, 2953–2963. [CrossRef]
6. Lee, J.G.; Jeon, O.S.; Hwang, H.J.; Jang, J.; Lee, Y.; Hyun, S.H.; Shul, Y.G. Durable and High-Performance Direct-Methane Fuel Cells with Coke-Tolerant Ceria-Coated Ni Catalysts at Reduced Temperatures. *Electrochim. Acta* **2016**, *191*, 677–686. [CrossRef]
7. Lee, D.; Myung, J.; Tan, J.; Hyun, S.-H.; Irvine, J.T.; Kim, J.; Moon, J. Direct methane solid oxide fuel cells based on catalytic partial oxidation enabling complete coking tolerance of Ni-based anodes. *J. Power Sources* **2017**, *345*, 30–40. [CrossRef]
8. Omar, A.F.; Othman, M.H.D.; Gunaedi, C.N.; Jamil, S.M.; Mohamed, M.H.; Jaafar, J.; Rahman, M.A.; Ismail, A.F. Performance analysis of hollow fibre-based micro-tubular solid oxide fuel cell utilising methane fuel. *Int. J. Hydrogen Energy* **2019**, *44*, 30754–30762. [CrossRef]
9. Riegraf, M.; Dierickx, S.; Weber, A.; Costa, R.; Schiller, G.; Friedrich, K.A. Electrochemical Impedance Analysis of Ni/CGO10-Based Electrolyte-Supported Cells. *ECS Trans.* **2019**, *91*, 1985–1992. [CrossRef]
10. Osinkin, D. Complementary effect of ceria on the hydrogen oxidation kinetics on Ni—$Ce_{0.8}Sm_{0.2}O_{2-\delta}$ anode. *Electrochim. Acta* **2020**, *330*, 135257. [CrossRef]
11. Öksüzömer, M.F.; Sarıboğa, V. Combined Cu-CeO_2/YSZ and Ni/YSZ dual layer anode structures for direct methane solid oxide fuel cells. *Int. J. Energy Res.* **2018**, *42*, 3228–3243. [CrossRef]
12. Rabuni, M.F.; Li, T.; Punmeechao, P.; Li, K. Electrode design for direct-methane micro-tubular solid oxide fuel cell (MT-SOFC). *J. Power Sources* **2018**, *384*, 287–294. [CrossRef]
13. Sumi, H.; Shimada, H.; Yamaguchi, T.; Fujishiro, Y.; Awano, M. Development of Portable Solid Oxide Fuel Cell System Driven by Hydrocarbon and Alcohol Fuels. *Adv. Bioceram. Porous Ceram. II* **2019**, *39*, 159–163.
14. Ab Rahman, M.; Othman, M.H.D.; Wibisono, Y.; Harun, Z.; Omar, A.F.; Shabri, H.A.; Deraman, S.; Rahman, M.A.; Jaafar, J.; Ismail, A.F. Effect of electrolyte thickness manipulation on enhancing carbon deposition resistance of methane-fueled solid oxide fuel cell. *Int. J. Energy Res.* **2021**, *45*, 2837–2855. [CrossRef]
15. Ab Rahman, M.; Othman, M.H.D.; Fansuri, H.; Harun, Z.; Omar, A.F.; Shabri, H.A.; Ravi, J.; Rahman, M.A.; Jaafar, J.; Ismail, A.F.; et al. Development of high-performance anode/electrolyte/cathode micro-tubular solid oxide fuel cell via phase inversion-based co-extrusion/co-sintering technique. *J. Power Sources* **2020**, *467*, 228345. [CrossRef]
16. Jamil, S.M.; Rahman, M.A.; Shabri, H.A.; Othman, M.H.D. Solid Electrolyte Membranes for Low- and High-Temperature Fuel Cells. In *Membrane Technology Enhancement for Environmental Protection and Sustainable Industrial Growth*; Zhang, Z., Zhang, W., Chehimi, M.M., Eds.; Springer International Publishing: Cham, Switzerland, 2021; pp. 109–125.
17. Eguchi, K.; Akasaka, N.; Mitsuyasu, H.; Nonaka, Y. Process of solid state reaction between doped ceria and zirconia. *Solid State Ionics* **2000**, *135*, 589–594. [CrossRef]
18. Tuller, H. Ionic conduction in nanocrystalline materials. *Solid State Ionics* **2000**, *131*, 143–157. [CrossRef]
19. Chen, J.; Carlson, B.D.; Toops, T.J.; Li, Z.; Lance, M.J.; Karakalos, S.G.; Choi, J.; Kyriakidou, E.A. Methane Combustion Over Ni/$Ce_xZr_{1-x}O_2$ Catalysts: Impact of Ceria/Zirconia Ratio. *ChemCatChem* **2020**, *12*, 5558–5568. [CrossRef]

20. Xu, H.; Cheng, K.; Chen, M.; Zhang, L.; Brodersen, K.; Du, Y. Interdiffusion between gadolinia doped ceria and yttria stabilized zirconia in solid oxide fuel cells: Experimental investigation and kinetic modeling. *J. Power Sources* **2019**, *441*, 227152. [CrossRef]
21. Kurapova, O.Y.; Shugurov, S.M.; Vasil'Eva, E.A.; Savelev, D.A.; Konakov, V.G.; Lopatin, S.I. Thermal prehistory, structure and high-temperature thermodynamic properties of Y_2O_3-CeO_2 and Y_2O_3-ZrO_2-CeO_2 solid solutions. *Ceram. Int.* **2021**, *47*, 11072–11079. [CrossRef]
22. Danielis, M.; Betancourt, L.E.; Orozco, I.; Divins, N.J.; Llorca, J.; Rodríguez, J.A.; Senanayake, S.D.; Colussi, S.; Trovarelli, A. Methane oxidation activity and nanoscale characterization of Pd/CeO_2 catalysts prepared by dry milling Pd acetate and ceria. *Appl. Catal. B Environ.* **2021**, *282*, 119567. [CrossRef]
23. Liu, Z.; Zhang, F.; Rui, N.; Li, X.; Lin, L.; Betancourt, L.E.; Su, D.; Xu, W.; Cen, J.; Attenkofer, K.; et al. Highly Active Ceria-Supported Ru Catalyst for the Dry Reforming of Methane: In Situ Identification of $Ru^{\delta+}$–Ce^{3+} Interactions for Enhanced Conversion. *ACS Catal.* **2019**, *9*, 3349–3359. [CrossRef]
24. Ahmad, S.I.; Rao, P.K.; Syed, I.A. Sintering temperature effect on density, structural and morphological properties of Mg- and Sr-doped ceria. *J. Taibah Univ. Sci.* **2016**, *10*, 381–385. [CrossRef]
25. Panthi, D.; Hedayat, N.; Du, Y. Densification behavior of yttria-stabilized zirconia powders for solid oxide fuel cell electrolytes. *J. Adv. Ceram.* **2018**, *7*, 325–335. [CrossRef]
26. Sariboğa, V.; Öksüzömer, M.F. Cu-CeO_2 anodes for solid oxide fuel cells: Determination of infiltration characteristics. *J. Alloys Compd.* **2016**, *688*, 323–331. [CrossRef]
27. Zhou, X. Electrical conductivity and stability of Gd-doped ceria/Y-doped zirconia ceramics and thin films. *Solid State Ionics* **2004**, *175*, 19–22. [CrossRef]
28. Mori, M.; Yamamoto, T.; Itoh, H.; Inaba, H.; Tagawa, H. Thermal Expansion of Nickel-Zirconia Anodes in Solid Oxide Fuel Cells during Fabrication and Operation. *J. Electrochem. Soc.* **1998**, *145*, 1374–1381. [CrossRef]
29. Wang, X.; Liu, T.; Wang, C.; Yu, J.; Li, L. Crystal structure, microstructure, thermal expansion and electrical conductivity of CeO_2–ZrO_2 solid solution. *Adv. Appl. Ceram.* **2017**, *116*, 477–481. [CrossRef]
30. Jamil, S.M.; Othman, M.H.D.; Rahman, M.A.; Jaafar, J.; Ismail, A.F.; Honda, S.; Iwamoto, Y. Properties and performance evaluation of dual-layer ceramic hollow fiber with modified electrolyte for MT-SOFC. *Renew. Energy* **2019**, *134*, 1423–1433. [CrossRef]
31. Feng, J.; Qiao, J.; Sun, W.; Yang, P.; Li, H.; Wang, Z.; Sun, K. Characteristic and preparation of $Ce_{0.5}Zr_{0.5}O_2$ as the anode support for solid oxide fuel cells by phase inversion technology. *Int. J. Hydrogen Energy* **2015**, *40*, 12784–12789. [CrossRef]
32. Dees, D.W.; Claar, T.D.; Easler, T.E.; Fee, D.C.; Mrazek, F.C. ChemInform Abstract: The Conductivity of Porous Ni/ZrO_2-Y_2O_3 Cermets. *Chemin* **1987**, *18*, 5–10. [CrossRef]
33. Yu, J.H.; Park, G.W.; Lee, S.; Woo, S.K. Microstructural effects on the electrical and mechanical properties of Ni–YSZ cermet for SOFC anode. *J. Power Sources* **2007**, *163*, 926–932. [CrossRef]
34. Sasaki, K.; Teraoka, Y. Equilibria in Fuel Cell Gases. *J. Electrochem. Soc.* **2003**, *150*, A885–A888. [CrossRef]
35. Shishkin, M.; Ziegler, T. Direct modeling of the electrochemistry in the three-phase boundary of solid oxide fuel cell anodes by density functional theory: A critical overview. *Phys. Chem. Chem. Phys.* **2014**, *16*, 1798–1808. [CrossRef] [PubMed]
36. Vita, A. Catalytic Applications of CeO_2-Based Materials. *Catalysts* **2020**, *10*, 576. [CrossRef]
37. Shutilov, A.A.; Simonov, M.N.; Zaytseva, Y.A.; Zenkovets, G.A.; Simakova, I. Phase composition and catalytic properties of ZrO_2 and CeO_2-ZrO_2 in the ketonization of pentanoic acid to 5-nonanone. *Kinet. Catal.* **2013**, *54*, 184–192. [CrossRef]
38. Coles-Aldridge, A.V.; Baker, R.T. Oxygen ion conductivity in ceria-based electrolytes co-doped with samarium and gadolinium. *Solid State Ionics* **2020**, *347*, 115255. [CrossRef]
39. Lasia, A. *Electrochemical Impedance Spectroscopy and Its Applications*; Springer: New York, NY, USA, 2014; ISBN 978-1-4614-8932-0. [CrossRef]
40. Luciani, G.; Landi, G.; Imparato, C.; Vitiello, G.; Deorsola, F.A.; Di Benedetto, A.; Aronne, A. Improvement of splitting performance of Ce0.75Zr0.25O_2 material: Tuning bulk and surface properties by hydrothermal synthesis. *Int. J. Hydrogen Energy* **2019**, *44*, 17565–17577. [CrossRef]
41. Deng, J.; Li, S.; Xiong, L.; Jiao, Y.; Yuan, S.; Wang, J.; Chen, Y. Preparation of nanostructured CeO_2-ZrO_2-based materials with stabilized surface area and their catalysis in soot oxidation. *Appl. Surf. Sci.* **2020**, *505*, 144301. [CrossRef]
42. Shishkin, M.; Ziegler, T. The Electronic Structure and Chemical Properties of a Ni/CeO_2 Anode in a Solid Oxide Fuel Cell: A DFT + U Study. *J. Phys. Chem. C* **2010**, *114*, 21411–21416. [CrossRef]
43. Escudero, M.; Serrano, J. Individual impact of several impurities on the performance of direct internal reforming biogas solid oxide fuel cell using W-Ni-CeO_2 as anode. *Int. J. Hydrogen Energy* **2019**, *44*, 20616–20631. [CrossRef]
44. Hou, X.; Zhao, K.; Marina, O.A.; Norton, M.G.; Ha, S. NiMo-ceria-zirconia-based anode for solid oxide fuel cells operating on gasoline surrogate. *Appl. Catal. B Environ.* **2019**, *242*, 31–39. [CrossRef]
45. Fuerte, A.; Valenzuela, R.X.; Escudero, M.J. Role of Dopants on Ceria-based Anodes for IT-SOFCs Powered by Hydrocarbon Fuels. *Univers. J. Electr. Electron. Eng.* **2017**, *5*, 45–55. [CrossRef]
46. Rudin, S.N.F.M.; Ab Muis, Z.; Ramli, A.F.; Shabri, H.A.; Zailan, R.; Hashim, H.; Ho, W.S. Sustainable Supply of Hydrogen for Integrated Power Plant with Methanation via Pinch Analysis. In *IOP Conference Series: Materials Science and Engineering*; IOP Publishing: Bristol, UK, 2020; Volume 884. [CrossRef]
47. Rudin, S.N.F.M.; Ab Muis, Z.; Hashim, H.; Ho, W.S. Techno-economic assessment of integrated power plant with methanation. *Chem. Eng. Trans.* **2018**, *63*, 451–456.